The Astrophysical Journal Supplement Series, 166:470–497, 2006 October

SPECTRAL ENERGY DISTRIBUTIONS AND MULTIWAVELENGTH SELECTION OF TYPE 1 QUASARS

Gordon T. Richards,[1,2] Mark Lacy,[3] Lisa J. Storrie-Lombardi,[3] Patrick B. Hall,[4] S. C. Gallagher,[5]
Dean C. Hines,[6] Xiaohui Fan,[7] Casey Papovich,[7] Daniel E. Vanden Berk,[8] George B. Trammell,[8]
Donald P. Schneider,[8] Marianne Vestergaard,[7] Donald G. York,[9,10] Sebastian Jester,[11,12]
Scott F. Anderson,[13] Tamás Budavári,[2] and Alexander S. Szalay[2]

Received 2006 January 24; accepted 2006 May 26

ABSTRACT

We present an analysis of the mid-infrared (MIR) and optical properties of type 1 (broad-line) quasars detected by the *Spitzer Space Telescope*. The MIR color-redshift relation is characterized to $z \sim 3$, with predictions to $z = 7$. We demonstrate how combining MIR and optical colors can yield even more efficient selection of active galactic nuclei (AGNs) than MIR or optical colors alone. Composite spectral energy distributions (SEDs) are constructed for 259 quasars with both Sloan Digital Sky Survey and *Spitzer* photometry, supplemented by near-IR, *GALEX*, VLA, and *ROSAT* data, where available. We discuss how the spectral diversity of quasars influences the determination of bolometric luminosities and accretion rates; assuming the mean SED can lead to errors as large as 50% for individual quasars when inferring a bolometric luminosity from an optical luminosity. Finally, we show that careful consideration of the shape of the mean quasar SED and its redshift dependence leads to a lower estimate of the fraction of reddened/obscured AGNs missed by optical surveys as compared to estimates derived from a single mean MIR to optical flux ratio.

Subject headings: catalogs — galaxies: active — infrared: galaxies — quasars: general — radio continuum: galaxies — surveys — ultraviolet: galaxies — X-rays: galaxies

Online material: machine-readable tables

1. INTRODUCTION

Access to the mid-infrared (MIR) region opens up new realms for quasar science as we are able to study large numbers of objects with high signal-to-noise ratio data in this bolometrically important band for the first time. At least four distinct energy generation mechanisms are at work in active galactic nuclei (AGNs) from jets in the radio, dust in the IR, accretion disks in the optical–UV–soft–X-ray, and Compton upscattering in hot coronae in the hard X-ray. All of these spectral regions need to be sampled with high precision if we are to understand the physical processes governing AGN emission. The *Spitzer Space Telescope* (Werner et al. 2004) allows the first robust glimpse of the physics of the putative dusty torus in AGNs out to $z \sim 2-3$ and makes it possible to compare high-quality mid-IR data to the expectations of the latest models (e.g., Nenkova et al. 2002; Dullemond & van Bemmel 2005; Fritz et al. 2006).

MIR photometry from *Spitzer* has provided a better census of active nuclei in galaxies than has been previously possible (e.g., Lacy et al. 2004). Optical surveys are biased against heavily reddened and obscured objects, and even X-ray surveys may fail to uncover Compton-thick sources (e.g., Treister et al. 2006). Thus, the MIR presents an attractive window for determining the black hole accretion history of the universe. To that end, *Spitzer* will be of considerable utility in helping to decipher the nature of the $M_{\rm BH}$-σ relation (e.g., Tremaine et al. 2002), in terms of making a complete census of AGNs—a necessary condition for a full understanding of the physical relationship between black holes and their host galaxies.

High-sensitivity, high-accuracy MIR photometry also fills a huge gap in our knowledge of the overall spectral energy distribution (SED) of AGNs, which now lacks only detailed far-IR/centimeter and extreme-UV measurements for a large sample of quasars. Without the mid-IR data, we have been forced to rely on the mean properties of a few dozen of the brightest quasars (e.g., Elvis et al. 1994) to estimate bolometric luminosities (and, in turn, Eddington masses and accretion rates) for quasars. Since the 1–100 μm part of the spectrum contributes nearly 40% of the bolometric luminosity, this added knowledge represents a significant gain in our ability to explore the properties of AGNs as a function of the bolometric luminosity.

This paper builds on and extends the results from recent papers describing the *Spitzer* MIR color distribution of AGNs. Lacy et al. (2004) showed that MIR colors alone can be used to select AGNs with both high efficiency and completeness, including both dust-reddened and optically obscured (type 2) AGNs that may otherwise be overlooked by optical selection techniques. We will show that the addition of optical colors and morphology can be used to improve the MIR-only selection efficiency of type 1 quasars (including those that are moderately reddened).

[1] Princeton University Observatory, Peyton Hall, Princeton, NJ 08544.
[2] Department of Physics and Astronomy, The Johns Hopkins University, 3400 North Charles Street, Baltimore, MD 21218-2686.
[3] *Spitzer* Science Center, California Institute of Technology, Mail Code 220-6, Pasadena, CA 91125.
[4] Department of Physics and Astronomy, York University, 4700 Keele Street, Toronto, ON M3J 1P3, Canada.
[5] Department of Physics and Astronomy, UCLA, Mail Code 154705, 475 Portola Plaza, Los Angeles, CA 90095.
[6] Space Science Institute, 4750 Walnut Street, Suite 205, Boulder, CO 80301.
[7] Steward Observatory, University of Arizona, 933 North Cherry Avenue, Tucson, AZ 85721.
[8] Department of Astronomy and Astrophysics, Pennsylvania State University, 525 Davey Laboratory, University Park, PA 16802.
[9] Department of Astronomy and Astrophysics, University of Chicago, 5640 South Ellis Avenue, Chicago, IL 60637.
[10] Enrico Fermi Institute, University of Chicago, 5640 South Ellis Avenue, Chicago, IL 60637.
[11] Fermi National Accelerator Laboratory, P.O. Box 500, Batavia, IL 60510.
[12] School of Physics and Astronomy, Southampton University, Southampton SO17 1BJ, UK.
[13] Department of Astronomy, University of Washington, Box 351580, Seattle, WA 98195.

Stern et al. (2005) also describe a MIR selection technique for AGNs, making statistical arguments that the obscured AGN fraction may be as high as 76%. We reconsider their argument in light of the influence that the shape of the mean quasar spectral energy distribution (SED) has on determining the obscured quasar fraction. Such considerations allow us to demonstrate that the true obscured AGN fraction must be lower than that determined by Stern et al. (2005).

Finally, Hatziminaoglou et al. (2005) investigated the combined optical + MIR color distribution of quasars by combining data from the ELAIS-N1 field in the *Spitzer* Wide-Area Infrared Extragalactic Survey (SWIRE; Lonsdale et al. 2003) with data from the Sloan Digital Sky Survey (SDSS; York et al. 2000). Using the data from 35 SDSS quasars they determine the mean optical-MIR SED of type 1 quasars and investigate their mass and bolometric luminosity distribution. We expand on these results by determining a number of different "mean" SEDs as a function of color and luminosity for 259 SDSS quasars in the *Spitzer* Extragalactic First Look Survey[14] (XFLS), SWIRE[15] ELAIS-N1/N2, and SWIRE Lockman Hole areas. We use these SEDs to demonstrate that the diversity of quasar SEDs must be considered when determining bolometric luminosities and accretion rates for individual quasars—as was emphasized in the seminal SED work of Elvis et al. (1994).

Section 2 reviews the data sets used in our analysis. In § 3 we explore the MIR color-redshift relation and MIR-optical color-color space occupied by type 1 quasars. In addition to showing these relations for the data, we also show the predicted relations derived from two quasar SEDs convolved with the SDSS and *Spitzer* filters curves: one SED derived largely from broadband photometry (Elvis et al. 1994), the other from a mean optical + IR spectral template (Glikman et al. 2006). Section 4 presents a brief discussion of the determination of the type 1 to type 2 ratio of quasars. In § 5 we discuss the radio through X-ray SED of quasars and construct new MIR-optical templates from our sample. We present an overall mean SED along with mean SEDs for subsets of optically luminous/dim, MIR luminous/dim, and optically blue/red quasars in order to explore how different optical/MIR properties are related to the overall SED. Section 6 discusses the implications of our new SED templates on the determination of bolometric luminosities and accretion rates. Our conclusions are presented in § 7.

Throughout this paper we will distinguish between normal type 1 quasars, dust-reddened/extincted type 1 quasars, and type 2 quasars. By "type 1 quasars," we mean those quasars having broad lines and optical colors/spectral indices that are roughly consistent with a Gaussian spectral index distribution of $\alpha_\nu = -0.5 \pm 0.3$ ($f_\nu \propto \nu^\alpha$). Reddened type 1 quasars are those quasars that have broad lines but have spectral indices that are redder than about $\alpha_\nu = -1$ (e.g., Gregg et al. 2002). Optical surveys can find such quasars up to $E(B-V) \sim 0.5$ but are increasingly incomplete above $E(B-V) \sim 0.1$ (Richards et al. 2003). By type 2 quasars, we mean those that lack rest-frame optical/UV broad emission lines and have nuclei that are completely obscured in the optical such that the optical colors are consistent with the host galaxy. Throughout this paper we use a ΛCDM cosmology with $H_0 = 70\ \mathrm{km\ s^{-1}\ Mpc^{-1}}$, $\Omega_\Lambda = 0.7$, and $\Omega_m = 0.3$, consistent with the *WMAP* cosmology (Spergel et al. 2003, 2006).

2. THE DATA

We investigate the mid-IR and optical properties of type 1 quasars that are detected in both the SDSS and in all four bands of the *Spitzer* Infrared Array Camera (IRAC; Fazio et al. 2004). The *Spitzer* data are taken from the XFLS and SWIRE ELAIS-N1, ELAIS-N2, and Lockman Hole areas, which have (R.A., decl.) centers of (259.°5, 59.°5), (242.°75, 55.°0), (249.°2, 41.°029), and (161.°25, 58.°0), respectively.

We begin with SDSS-DR3 type 1 quasars cataloged by Schneider et al. (2005), the majority of which were selected by the algorithm given by Richards et al. (2002). This catalog includes matches to the FIRST (Becker et al. 1995) survey with the VLA, *ROSAT* (Voges et al. 2000), and 2MASS (Skrutskie et al. 1997). For a definition of the SDSS photometric system, see Fukugita et al. (1996); Adelman-McCarthy et al. (2006) provide a description of the latest SDSS data release (DR4). All SDSS magnitudes have been corrected for Galactic extinction according to Schlegel et al. (1998).

The 46,420 SDSS quasars of Schneider et al. (2005) are matched to IRAC detections in the XFLS (main_4band.cat; Lacy et al. 2005b) and the SWIRE ELAIS-N1, -N2, and Lockman Hole (SWIRE2_N1_cat_IRAC24_16jun05.tbl, SWIRE2_N2_cat_IRAC24_16jun05.tbl, SWIRE2_Lockman_cat_IRAC24_10Nov05.tbl; Surace et al. 2005) areas of sky. The IRAC bandpasses are generally referred to as channels 1 through 4 or as the 3.6, 4.5, 5.8, and 8.0 μm bands, respectively. For a quasar spectrum with MIR spectral index of $\alpha_\nu = -1$ ($f_\nu \propto \nu^\alpha$), the effective wavelengths of the IRAC bandpasses are actually closer to 3.52, 4.46, 5.67, and 7.70 μm. The SWIRE catalogs also include 24 μm photometry from the Multiband Imaging Photometer for *Spitzer* (MIPS; Rieke et al. 2004). In the XFLS field, 24 μm sources are cataloged by Fadda et al. (2006) and we include matches from that catalog as well. As the limits of the mid-IR catalogs are much deeper than the SDSS spectroscopic survey, we consider only objects detected in all four IRAC bands. Within a matching radius of 1.″0 there are 44 SDSS-DR3 quasar matches in the XFLS area, 29 in the ELAIS-N1 area, 44 in the ELAIS-N2 area, and 142 in the Lockman Hole area. All but one of the optically selected SDSS quasars has four-band IRAC coverage in the regions of overlap between the SDSS and *Spitzer* data; see Figures 1 and 2. The exception is SDSS J104413.47+580858.9 ($z = 3.7$), which has only a limit in IRAC channel 3.

To construct the most detailed quasar spectral energy distributions (SEDs) possible, we include data available at other wavelengths. We include matches to MIPS 70 μm sources in the XFLS (FLS70_sn7_jul05.txt; Frayer et al. 2006) and in the SWIRE (SWIRE2_EN1_70um_23nov05.tbl, SWIRE2_EN2_70um_23nov05.tbl, SWIRE3_Lockman_70um_23nov05.tbl; Surace et al. 2005) areas. No MIPS 160 μm data are included as the flux density limits of these data in the XFLS and SWIRE areas are much brighter than expected flux densities of even the brightest SDSS-DR3 quasars in these fields. For the SDSS quasars in the ELAIS fields we have extracted 15 μm photometry from the Rowan-Robinson et al. (2004) catalog. We also extract $J/H/K$ and radio information from this catalog if that information was not otherwise available.

Some of these areas of sky have been observed by *GALEX* (Martin et al. 2005), and the data were released as part of *GALEX* GR1. Quasars are readily detected by *GALEX* (see Bianchi et al. 2005 and Seibert et al. 2005); thus, we also include *GALEX* photometry where available. Matching of the *GALEX* catalogs and the SDSS DR3 quasar sample is described by Trammell et al. (2005). The effective wavelengths of the *GALEX* NUV and FUV bandpasses (hereafter referred to as n and f magnitudes) are 2267 and 1516 Å. *GALEX* photometry has been corrected for Galactic extinction assuming $A_n/E(B-V) = 8.741$ and $A_f/E(B-V) = 8.376$ (Wyder et al. 2005). A total of 55 and 88

[14] See http://ssc.spitzer.caltech.edu/fls/.
[15] See http://swire.ipac.caltech.edu/swire/.

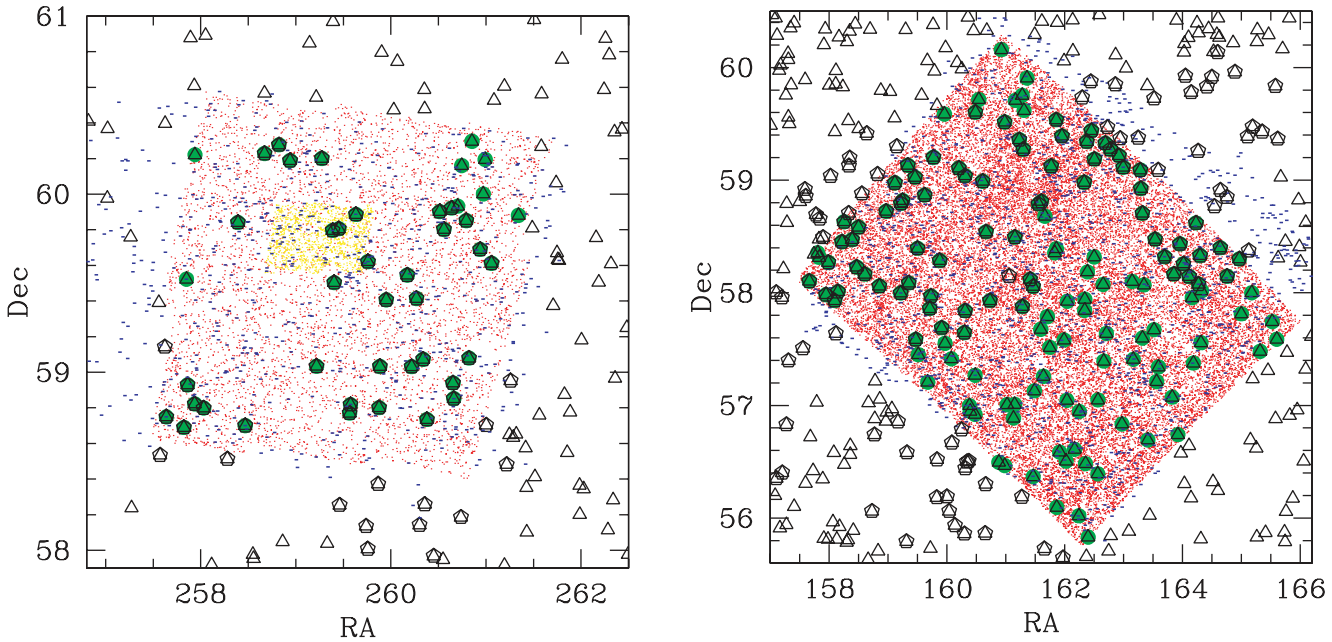

FIG. 1.—Location of SDSS-DR3 quasars in the XFLS (*left*) and SWIRE Lockman Hole (*right*) fields. Red, yellow, and blue points represent IRAC, IRAC verification, and MIPS70 sources, respectively. Open triangles represent SDSS-DR3 quasars. Green circles represent SDSS-DR3 quasars with IRAC detections in all four bands. Open pentagons indicate *GALEX*-detected SDSS quasars.

of the DR3 quasars have *GALEX* detections in the *f* and *n* bands, respectively.

In the radio, we have matched to the deeper VLA data taken in the XFLS area by Condon et al. (2003), which catalogs 5 σ detections with fluxes higher than 115 μJy (about an order of magnitude deeper than FIRST). Deep VLA data also exists for the ELAIS and Lockman Hole areas, but only over a small area of sky (e.g., Ciliegi et al. 1999, 2003).

Most of our objects are fainter than the 2MASS (Skrutskie et al. 1997) limits, but we have supplemental near-IR data for a few. Near-IR (JHK_s) magnitudes for SDSS J1716+5902 were obtained on 2003 September 9 UT using the GRIM II instrument on the Apache Point Observatory 3.5 m telescope. Dithered images were obtained and reduced in the standard fashion, using running flat-fielding and sky-subtraction (e.g., Hall et al. 1998) with all available good images in a given filter for each object. Four other sources (SDSS J171732.94+594747.5, SDSS J171736.90+593011.4, SDSS J171748.43+594820.6, and SDSS J171831.73+595309.4) were observed at Palomar Observatory.

Finally, to better characterize the optical + MIR color distribution of type 1 quasars, we include 87 broadline quasars that are fainter than the SDSS spectroscopic magnitude limit, but that

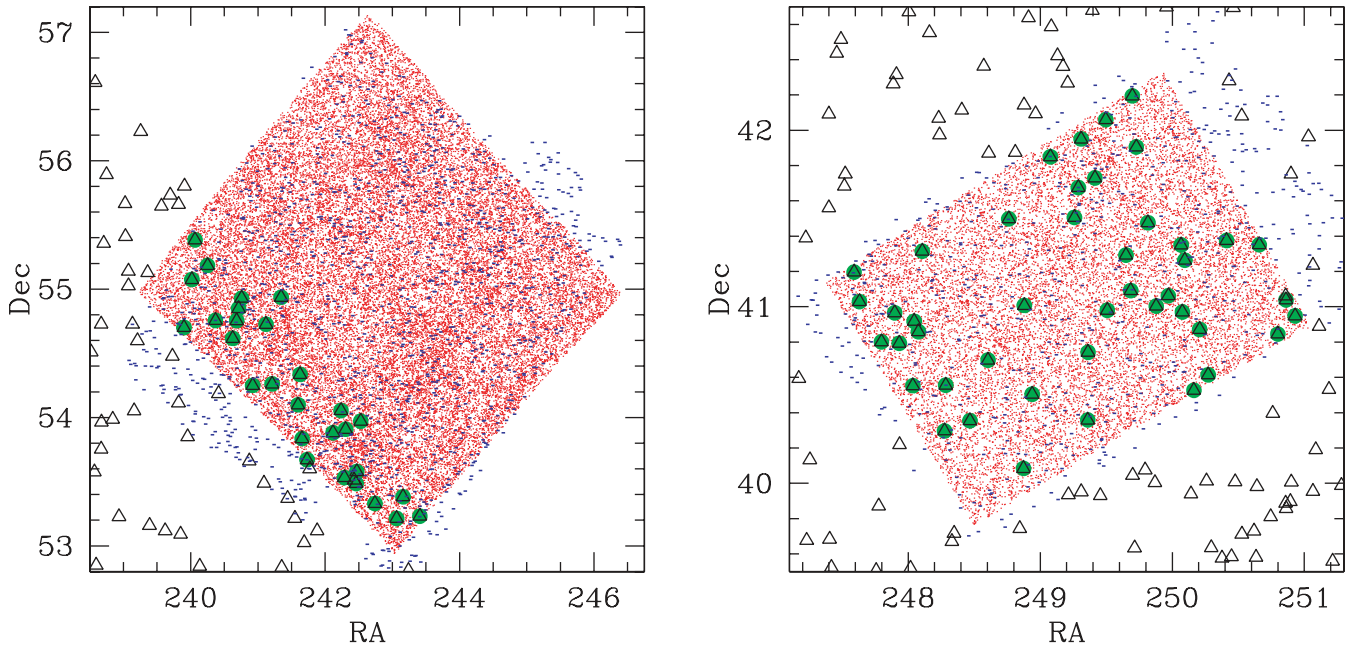

FIG. 2.—Location of SDSS-DR3 quasars in the SWIRE ELAIS N1 (*left*) and N2 (*right*) fields. Red points indicate four-band IRAC sources. Blue points indicate MIPS 70 μm sources. Open triangles indicate SDSS-DR3 quasars. Green circles indicate SDSS-DR3 quasars with IRAC detections in all four bands.

TABLE 1

SDSS-*Spitzer* Quasar Photometry I

Name (SDSS J)	z_{em}	L_{bol}[a] log (ergs s^{-1})	L_{opt}[b] log (ergs s^{-1})	L_{ir}[c] log (ergs s^{-1})	BC[a]	X-Ray log (counts s^{-1})	f (AB mag)	n (AB mag)	u (AB mag)	g (AB mag)	r (AB mag)	i (AB mag)	z (AB mag)
105705.39+580437.4	0.140	45.06	44.49	44.78	10.60	−0.708	18.31 ± 0.08	18.15 ± 0.04	17.92 ± 0.03	17.61 ± 0.05	17.25 ± 0.02	16.83 ± 0.02	16.56 ± 0.04
171902.28+593715.9	0.178	45.21	44.74	44.93	9.41	−1.221	18.10 ± 0.01	17.99 ± 0.01	17.49 ± 0.02	17.50 ± 0.02	17.36 ± 0.02	17.06 ± 0.02	17.20 ± 0.02
160655.34+534016.8	0.214	45.13	44.45	44.91	11.87	...	...	...	18.85 ± 0.03	18.71 ± 0.02	18.22 ± 0.02	17.86 ± 0.02	17.91 ± 0.03
163111.28+404805.2.....	0.258	45.68	45.27	45.19	9.84	−0.551	...	...	16.98 ± 0.01	17.05 ± 0.02	17.08 ± 0.01	17.10 ± 0.01	16.86 ± 0.01
171207.44+584754.4	0.269	45.49	45.06	45.12	12.29	−1.235	17.97 ± 0.01	18.08 ± 0.01	17.83 ± 0.02	17.93 ± 0.02	17.88 ± 0.02	17.94 ± 0.02	17.51 ± 0.02
171033.21+584456.8	0.281	45.15	44.46	44.95	10.44	...	20.59 ± 0.04	20.06 ± 0.02	19.58 ± 0.03	19.25 ± 0.03	18.70 ± 0.02	18.52 ± 0.02	18.10 ± 0.03
105644.52+572233.4	0.286	45.08	44.53	44.78	10.12	...	...	...	19.36 ± 0.03	19.26 ± 0.02	18.88 ± 0.02	18.69 ± 0.02	18.32 ± 0.02
104739.49+563507.2	0.303	45.19	44.66	44.88	9.82	...	...	...	19.16 ± 0.04	19.02 ± 0.04	18.72 ± 0.04	18.57 ± 0.03	18.20 ± 0.03
155936.13+544203.8	0.308	45.42	44.87	45.15	11.75	...	...	...	18.55 ± 0.03	18.42 ± 0.04	18.27 ± 0.02	18.38 ± 0.03	17.87 ± 0.03
105626.96+580843.1	0.342	45.29	44.66	45.03	8.40	...	...	21.50 ± 0.20	19.45 ± 0.03	18.95 ± 0.02	18.57 ± 0.03	18.46 ± 0.02	17.88 ± 0.02

Note.—Table 1 is available in its entirety in the electronic edition of the *Astrophysical Journal Supplement*. A portion is shown here for guidance regarding its form and content.

[a] Bolometric (100 μm to 10 keV) luminosity and bolometric correction (from 5100 Å).

[b] 1–0.1 μm integrated luminosity.

[c] 100–1 μm integrated luminosity.

TABLE 2

SDSS-*Spitzer* Quasar Photometry II

Name (SDSS J)	J (Vega)	H (Vega)	K (Vega)	$S_{3.6}$ (μJy)	$S_{4.5}$ (μJy)	$S_{5.8}$ (μJy)	$S_{8.0}$ (μJy)	S_{15} (mJy)	S_{24} (mJy)	S_{70} (mJy)	Radio (mJy)	$L_{\rm rad}$ log (ergs s^{-1} Hz^{-1})
105705.39+580437.4	14.99 ± 0.08	14.21 ± 0.09	13.48 ± 0.07	2351.5 ± 5.6	2366.9 ± 7.3	2838.0 ± 15.1	6273.4 ± 16.1	...	16.61 ± 0.02	98.0 ± 0.6	...	<29.69
171902.28+593715.9	15.89 ± 0.09	15.02 ± 0.09	14.15 ± 0.06	2925.1 ± 293.1	4095.1 ± 409.8	5365.6 ± 541.1	7193.8 ± 720.4	...	26.91 ± 0.04	22.9 ± 4.0	0.23	29.28
160655.34+534016.8	16.37 ± 0.10	15.33 ± 0.11	14.32 ± 0.07	1396.7 ± 4.6	1657.2 ± 5.7	2047.6 ± 14.1	2973.1 ± 10.9	7.72	14.80 ± 0.02	37.7 ± 1.6	...	<30.09
163111.28+404805.2.....	16.24 ± 0.10	15.45 ± 0.12	14.48 ± 0.09	2729.7 ± 5.0	3632.2 ± 6.6	4686.4 ± 15.1	6218.9 ± 11.9	...	16.90 ± 0.03	...	...	<30.26
171207.44+584754.4	16.26 ± 0.10	15.36 ± 0.09	14.61 ± 0.10	2024.6 ± 203.1	2411.9 ± 242.2	3162.9 ± 321.5	4353.7 ± 437.9	...	13.34 ± 0.07	...	0.14	29.45
171033.21+584456.8	16.90 ± 0.18	15.68 ± 0.11	14.96 ± 0.10	589.2 ± 59.9	708.4 ± 71.8	709.8 ± 78.1	1571.6 ± 159.5	...	6.06 ± 0.07	44.0 ± 8.0	...	<30.34
105644.52+572233.4	16.71 ± 0.10	16.33 ± 0.27	15.10 ± 0.12	1161.4 ± 4.4	1280.1 ± 5.2	1417.1 ± 13.2	1742.5 ± 9.7	...	3.18 ± 0.02	...	...	<30.36
104739.49+563507.2	16.63 ± 0.16	16.24 ± 0.24	15.51 ± 0.18	572.2 ± 2.6	671.2 ± 2.6	886.3 ± 10.7	1566.3 ± 6.5	...	8.61 ± 0.02	...	...	<30.41
155936.13+544203.8	16.61 ± 0.20	16.77 ± 0.10	14.92 ± 0.16	1093.4 ± 2.6	1437.4 ± 3.8	1997.8 ± 8.6	3268.1 ± 8.7	...	14.59 ± 0.02	...	3.40	30.96
105626.96+580843.1	16.74 ± 0.17	16.25 ± 0.27	15.42 ± 0.16	1362.5 ± 5.2	1660.5 ± 4.9	1975.0 ± 15.5	2303.3 ± 9.0	...	4.23 ± 0.02	...	...	<30.53

Note.—Table 2 is available in its entirety in the electronic edition of the *Astrophysical Journal Supplement*. A portion is shown here for guidance regarding its form and content.

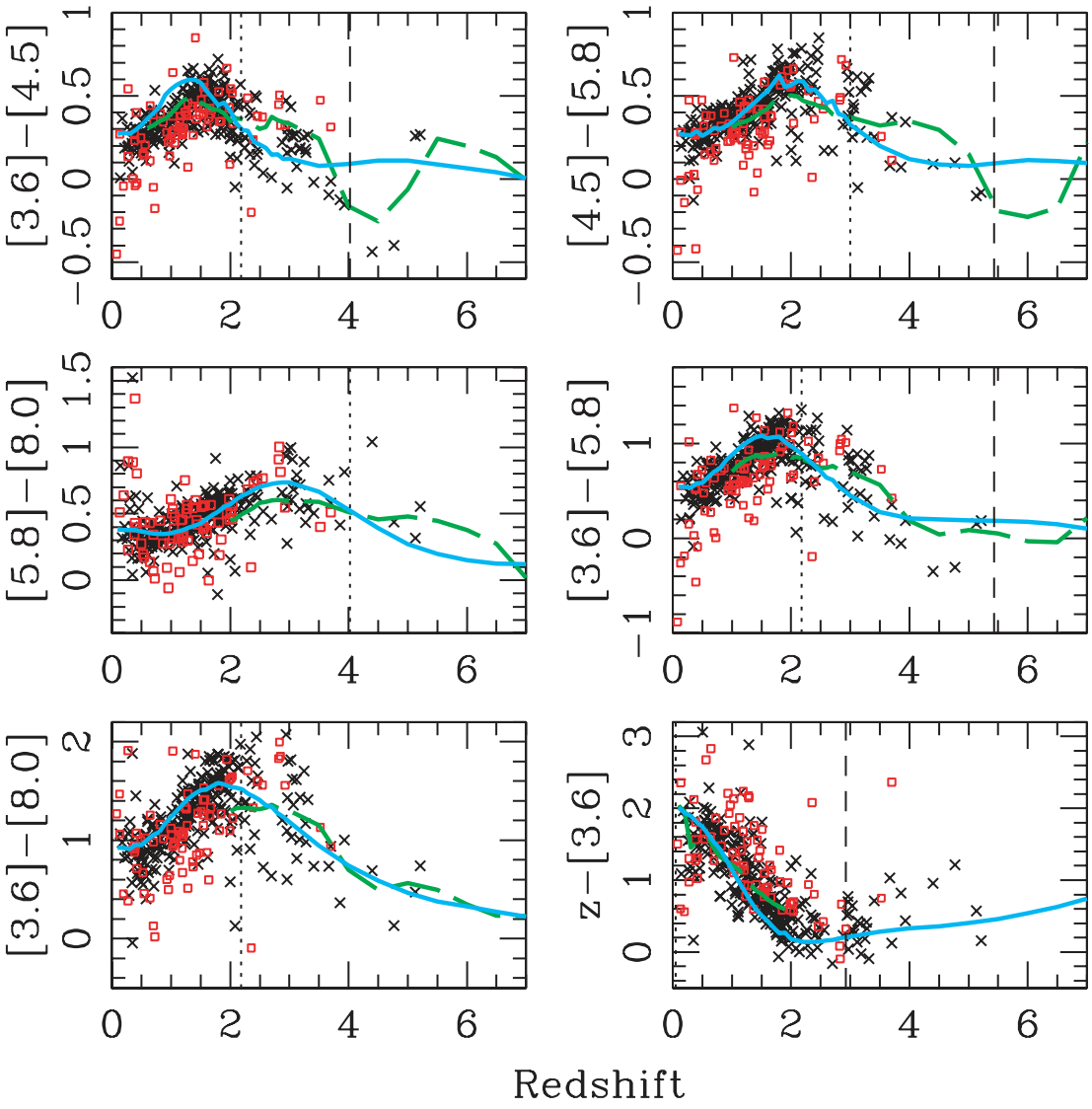

FIG. 3.—Color-redshift relation for various combinations of *Spitzer* colors. Black symbols represent SDSS-DR3 quasars from the XFLS and SWIRE ELAIS-N1/N2 and Lockman Hole areas. Open red squares represent Hectospec-confirmed XFLS quasars (Papovich et al. 2005). Errors are typically ~0.14 mag. The dashed green curve indicates the locus of synthetic colors determined from convolving the (redshifted) geometric mean of the optical-IR composite spectrum of Glikman et al. (2006) with the *Spitzer* IRAC transmission curves. The solid cyan curve shows the expected relation from convolving the Elvis et al. (1994) composite radio-quiet SED with the transmission curves. The vertical lines mark the redshifts where 1 μm enters the bluest (*dotted*) and leaves the reddest (*dashed*) band.

were confirmed from Hectospec (Fabricant et al. 2005) follow-up of MIPS 24 μm sources by Papovich et al. (2005).

Tables 1 and 2 present all of the multiwavelength data for the SDSS-DR3 quasars in our sample. The columns in Table 1 are name, redshift, bolometric luminosity (see § 6), integrated optical luminosity, integrated IR luminosity, bolometric correction (from rest-frame 5100 Å to the bolometric luminosity), X-ray (*ROSAT*) count rate, *GALEX f*- and *n*-band magnitudes/errors, and SDSS *ugriz* magnitudes/errors. The columns in Table 2 are name (again), *JHK* magnitudes/errors, *Spitzer* IRAC 3.6, 4.5, 5.8, and 8.0 μm flux densities/errors, *ISO* 15 μm flux density, *Spitzer* MIPS 24 and 70 μm flux densities/errors, radio (VLA, 20 cm) flux density, and radio luminosity. Both Tables 1 and 2 report only the observed Galactic-extinction corrected photometry of these sources; no host galaxy contamination has been removed (see § 5.2). Of these 259 quasars, 28 have *ROSAT* detections and 30 have radio detections. Of the 30 radio detections, only 8 are radio loud ($L_{\rm rad} > 10^{33}$ ergs s^{-1} Hz^{-1}).

3. MIR/OPTICAL COLORS OF TYPE 1 QUASARS

Lacy et al. (2004), Stern et al. (2005), and Hatziminaoglou et al. (2005) have already demonstrated that MIR selection of AGNs (both type 1 and type 2) from *Spitzer* photometry is very efficient. Here we demonstrate that this capability can be enhanced by including morphology and optical color information from SDSS. We concentrate on relatively unobscured type 1 quasars, but to the extent that dust-reddened type 1 quasars and obscured type 2 quasars are not extincted beyond the SDSS flux density limits, what we learn here will apply to those objects as well.

3.1. *The Color-Redshift Relations*

We begin by exploring the color-redshift relation for confirmed type 1 quasars. Figure 3 shows the color-redshift relation in various combinations of *Spitzer* colors for the SDSS-DR3 quasars from the XFLS and SWIRE ELAIS-N1/N2 and Lockman Hole

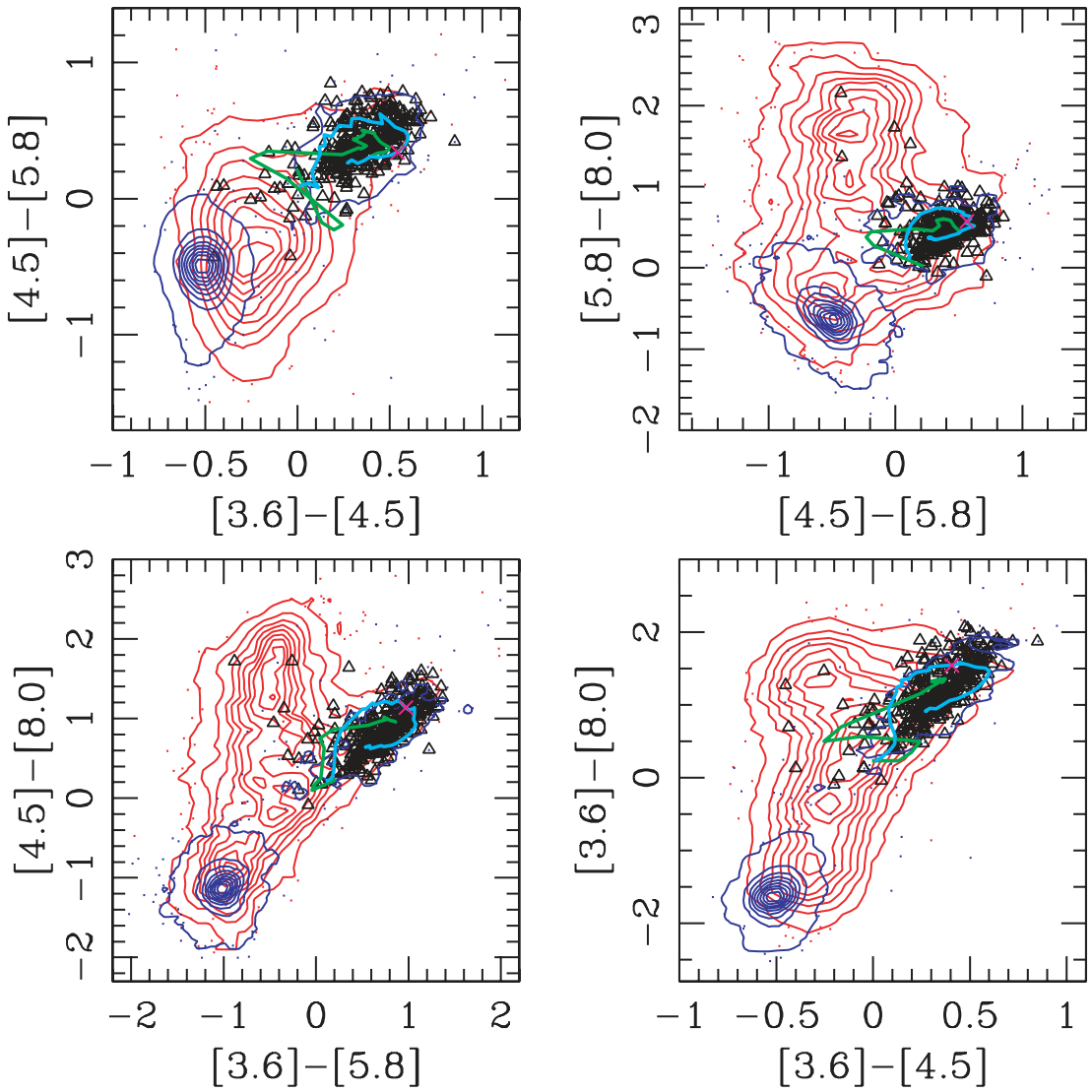

FIG. 4.—IRAC colors of SDSS + *Spitzer* objects. Blue contours and dots correspond to objects that have pointlike SDSS morphologies, while objects classified by the SDSS as extended are shown by red contours and dots. These blue and red contours/dots represent all of the objects detected in all four IRAC bands in the XFLS catalogs that have a match in the SDSS-DR3 photometric database. Note that point sources (*blue contours*) occupy two distinct regions corresponding to stars in the lower left of each panel and quasars in the upper right of each panel (the latter having just one contour level). Black triangles indicate spectroscopically confirmed type 1 quasars. The few outliers are from the Hectospec sample and may be mis-classified (or host galaxy dominated). The cyan lines represent the $z = 0.1$ to $z = 7$ colors predicted from the Elvis et al. (1994) quasar SED; the highest redshift quasars are at the blue (negative) end of the tracks. The green line shows the predicted colors from $z = 2$ ($z = 1$ in the top left panel) to $z = 7$ using the Glikman et al. (2006) composite spectrum. A magenta cross indicates where the lowest redshift from the Glikman et al. (2006) colors falls on the Elvis et al. (1994) curves. Redder colors have more positive values in this representation.

areas; see Richards et al. (2003, Fig. 2) for similar plots using the SDSS bands. The *Spitzer* colors are given in AB magnitude units where $[1] - [2] = -2.5 \log (S_1/S_2)$. Much of the color change seen in Figure 3 results from a single strong feature in the typical quasar SED—the so-called 1 μm inflection, where the slope of the SED changes sign in a νf_ν versus ν representation. Thus, we have indicated (by dotted and dashed lines, respectively) where the 1 μm inflection enters the bluest and leaves the reddest band. We extend the plot well beyond the redshifts of our confirmed quasars since *Spitzer* should be sensitive to quasars with redshifts in excess of $z = 7$, and it is helpful to know the expected colors of such objects.

We show two sets of predicted color-redshift relations in Figure 3 since, while the Elvis et al. (1994) quasar template covers the full redshift range, it is based in part on broadband photometry, which smears out the effects of the emission lines. The curves derived from the *spectroscopic* optical/MIR quasar template of Glikman et al. (2006) will be more accurate in regions of strong emission lines, but this template covers a smaller wavelength (and thus redshift) range. The discrepancy between the two predicted color-redshift relations at $z \sim 3$ and $z \sim 4.5$ in the $[3.6] - [4.5]$ color results from the Hα line moving into and out of the filters. Colors derived from nonadjacent bandpasses show a much smaller effect as the emission lines are not simultaneously moving out of the bluer band and into the redder band. The smoothness of the color-redshift relations (as compared to the SDSS) and the relatively large ($\sim$10%) photometric errors means that IRAC colors alone may not be useful for accurate quasar photometric redshift estimation (e.g., Richards et al. 2001; Weinstein et al. 2004), but MIR color information in addition to optical colors will be extremely useful in breaking redshift degeneracies in the optical. Note in particular the very large change in $z - [3.6]$ color between redshifts 0 and 2 as the 1 μm inflection moves between those two bandpasses.

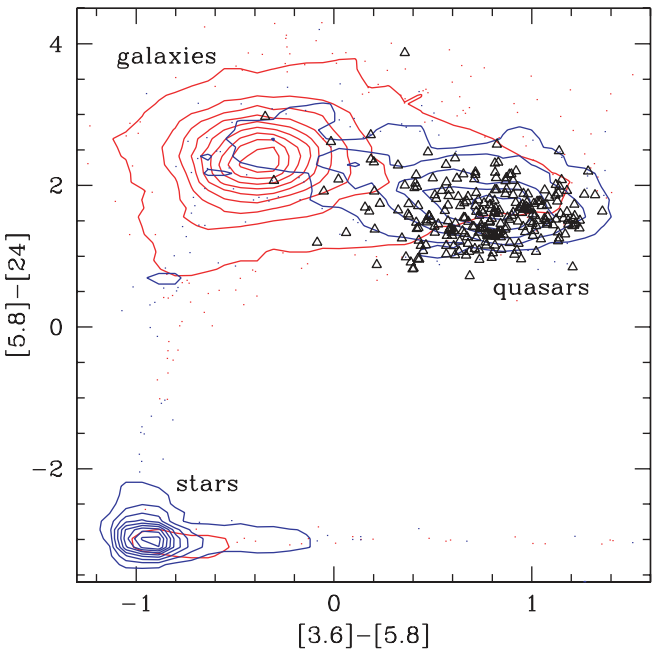

FIG. 5.—[3.6] − [5.8] vs. [5.8] − [24] colors of SDSS + *Spitzer* objects in the ELAIS areas. Contours and points are as in Fig. 4. Stars (which have very blue [5.8] − [24] color and generally have pointlike SDSS morphology classification) are much more cleanly separated from quasars and galaxies when the MIPS 24 μm data is included. However, little is gained in terms of galaxy-quasar separation as they have similarly red [5.8] − [24] colors.

3.2. *The Color-Color Relation and MIR + Optical Selection of AGNs*

We next examine the distribution of type 1 quasars in color-color space. Lacy et al. (2004), Stern et al. (2005), and Hatziminaoglou et al. (2005) have shown that AGNs can be selected using only MIR colors such as those plotted in Figure 4. From these plots, especially [3.6] − [5.8] versus [4.5] − [8.0] in the lower left-hand corner, it is clear that MIR colors combined with optical morphology can select type 1 quasars efficiently (and with a high degree of completeness) as pointlike sources (blue contours) with red MIR colors (e.g., more positive [3.6]−[5.8] color). Luminous type 2 quasar candidates can also be identified as those extended optical sources with AGN-like MIR colors. Adding the optical morphology information confirms the speculation of Lacy et al. (2004) and Stern et al. (2005) regarding the nature of the two red branches, with pointlike AGNs dominating the objects with red [3.6] − [5.8] color and extended sources (presumably low-redshift, PAH-dominated galaxies) populating the red [4.5] − [8.0] branch. Adding this SDSS morphology information thus enhances the MIR color-classification of sources since the *Spitzer* PSF is too large to yield morphology information for distant sources. We further demonstrate the classification information that is gained by including morphology in Figure 5, where we add MIPS 24 μm data in order to show [3.6] − [5.8] versus [5.8] − [24]. Adding the longer wavelength MIPS information clearly helps to discriminate stars (which have very blue [5.8] − [24] colors) from galaxies and quasars (which have very red [5.8] − [24] color); however, little is gained in terms of quasar-galaxy separation that was not already realized with the IRAC photometry.

While Hatziminaoglou et al. (2005) investigate both the MIR and optical colors of their sample, the combined optical + MIR colors are not considered for selection. This is appropriate given that the flux density limits of the *Spitzer* survey fields are much deeper than the spectroscopic limit of SDSS quasar survey (for a typical quasar SED) and the IR is much less affected by dust extinction (and thus is more representative of the quasar population at a given nuclear magnitude). However, the SDSS photometry goes more than 3 mag deeper than most of the SDSS's spectroscopic survey for quasars, and at $i = 21$, quasars must be reddened by $E(B - V) \sim 0.57$ to be extincted out of the SDSS imaging in the i band. As such, it is interesting to explore the selection of quasars using the combined SDSS plus *Spitzer* color information.

Figure 6 shows the color-space distribution of our sources using an SDSS color, an SDSS + *Spitzer* color, and a *Spitzer* color. For the SDSS color, we choose $g - i$ since those are the most widely

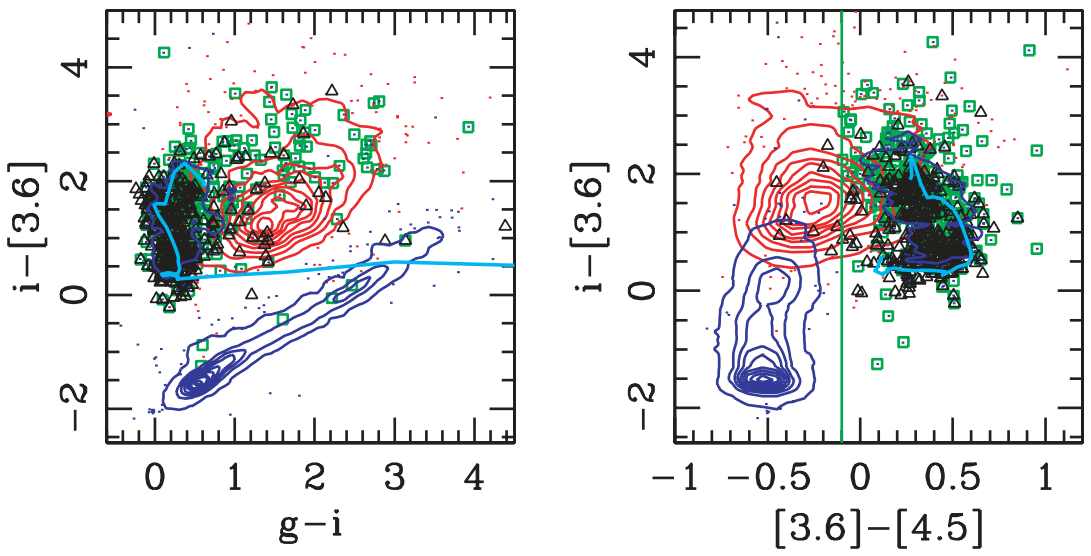

FIG. 6.—Color-color matrix using an SDSS color ($g - i$), an SDSS + *Spitzer* color ($i - [3.6]$), and a *Spitzer* color ([3.6] − [4.5]). See Fig. 4 for an explanation of the plot symbols. Combining *Spitzer* IRAC photometry with SDSS colors/morphology defines a parameter space where stars, AGNs, and normal galaxies can be efficiently distinguished. The green line in the right panel shows a possible selection criterion for unresolved AGNs; open green squares show the point sources selected by such a cut. Black triangles are confirmed SDSS quasars. The cyan line shows the expected colors of quasars from $z = 0.1$ to $z = 5$ (using the Elvis et al. 1994 mean SED); low-redshift quasars having the reddest $i - [3.6]$ colors. The contours and dots are for XFLS sources only, whereas the black and green symbols are drawn from all four areas of sky in our sample.

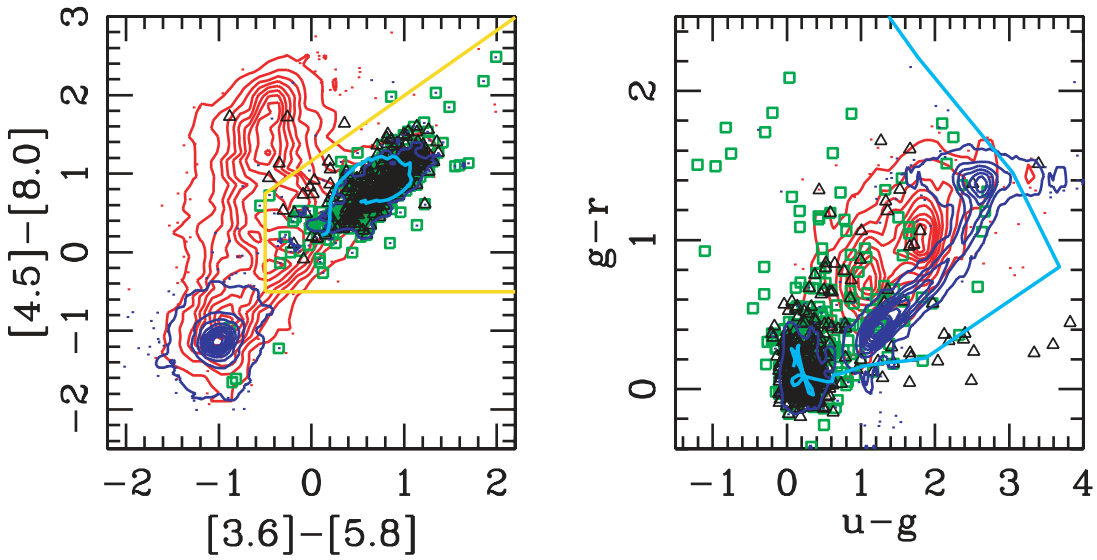

FIG. 7.—MIR (*left*) and optical (*right*) color-color plots showing the location of optical-color/morphology + MIR-color selected populations. See Fig. 4 for an explanation of the plot symbols. Quasar candidates (see Fig. 6) are shown as open green squares. The yellow lines in the left panel show the MIR selection criteria from Lacy et al. (2004), after having multiplied their cuts by 2.5 to convert to a magnitude scale.

separated high S/N bands in the SDSS filter set. For SDSS + *Spitzer*, we chose the two closest high S/N bands (i and $S_{3.6}$). For the *Spitzer* color, we chose the two highest S/N bands ($S_{3.6}$ and $S_{4.5}$); this choice happens to produce the greatest separation of classes and has the added attraction that it does not rely on the longer wavelength bands that will be lost when *Spitzer*'s coolant runs out. This presentation shows that AGNs, normal galaxies, and stars can be separated quite cleanly when using both optical and near-IR information, particularly when morphology information is available in addition to the colors. If we were simply interested in selecting type 1 quasars, then selecting point sources with $[3.6] - [4.5] > -0.1$ might be sufficient given that such a cut includes nearly all of the point sources with nonstellar colors (with the exception of quasars near $z = 4.5$; see Fig. 3). However, the morphology issue is complex. Including morphology means that normal galaxies will not contaminate the sample, but that type 2 AGNs and faint AGNs with extended or poorly determined morphologies will be lost. Judicious rotation of the axes in Figure 6 may allow for relatively clean AGN selection without having to rely on morphology information. However, a better approach would be to take advantage of the eight-dimensional color space afforded by SDSS and *Spitzer* photometry and performing a Bayesian classification such as the kernel density estimation algorithm described by Richards et al. (2004). We intend to pursue such an approach in a future publication.

We can compare this optical + MIR selection to the MIR-only selection of Lacy et al. (2004), Stern et al. (2005), and Hatziminaoglou et al. (2005). Each of these papers uses slightly different MIR selection techniques. We will compare explicitly only to Lacy et al. (2004) as their selection is seen to empirically produce the greatest color separation with respect to morphology. In the left-hand panel of Figure 7 we reproduce the $[3.6] - [5.8]$ versus $[4.5] - [8.0]$ color-color plot from Lacy et al. (2004), showing their selection as yellow lines. Objects selected as being optical point sources with red MIR colors are shown as open green squares. Adding the optical data to the selection criteria allows us to select quasars more efficiently by removing normal galaxies from the MIR-only color-selected region, but with reduced completeness due to the loss of AGNs dominated by host galaxy light in the optical. The right-hand panel of Figure 7 shows where these objects lie in $u - g$ versus $g - r$ color space. For the sake of clarity, we have limited the point and extended sources to $g < 21$ to reduce the scatter due to SDSS photometric error, but the green squares (pointlike quasar candidates) have no such limit applied.

We note that, despite the MIR color selection, the green squares are still predominantly UV-excess sources. To $i < 21$, we find that 70% of the MIR color-selected quasars have $u - g < 0.6$ and $g - r < 0.6$. Thus, the fraction of dust-reddened/extincted type 1 quasars (e.g., Richards et al. 2003; Glikman et al. 2004) that might be missed by an optical survey with UVX color-selection is no larger than 30%. This limit applies to quasars with i-band extinction less than 1.0 mag (the difference between the SDSS i-band imaging limit and our adopted cut of $i = 21$), which is $E(B - V) = 0.48$ for Galactic extinction. This fraction may be higher if there are type 1 quasars with larger extinction but is most likely smaller than 30% since many of the non-UVX quasars will simply have $z \gtrsim 2.2$. Quasars with $z > 2.2$ have redder optical colors even if they are not dust-reddened, and a large fraction of this population will still be identified by the SDSS quasar-selection algorithm.

Figure 8 shows color-magnitude plots corresponding to the color-color plots in Figures 6 and 7. The 3.6 μm flux density is limited for $[3.6] - [4.5] < 0.0$ by the 8.0 μm flux density limit and for $0.0 < [3.6] - [4.5] < 0.8$ by the 5.8 μm flux density limit, as shown by the dashed lines. Note that, while the 3.6 μm flux density limit is 20 μJy, a 3.6 μm selected sample is complete to all AGNs to only $\sim$200 μJy with a four-band IRAC selection criterion for a typical quasar SED in the mid-IR. This figure also serves to illustrate that MIR-only selection is most efficient for bright MIR sources. For $S_{3.6} > 1$ mJy there is little contamination of the MIR color space of AGNs, but at fainter limits, contamination from star-forming galaxies becomes problematic without additional selection information (such as the optical morphology). In the right-hand panel we again see that the density of dust-reddened and extincted type 1 quasars cannot be too large since the density of quasars with $i < 19$ and $g - i < 0.8$ is much higher than that of $i < 22$ quasar candidates with $g - i > 0.8$.

We can summarize this section as follows. MIR-only selection of AGNs such as described by Lacy et al. (2004) and shown in

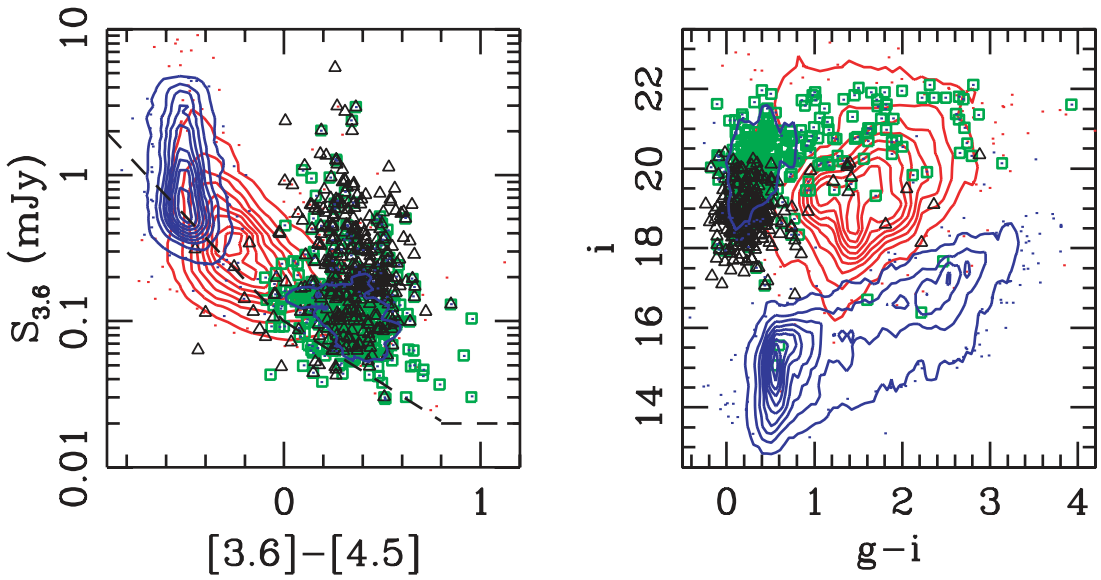

FIG. 8.—*Left*: *Spitzer* color-magnitude diagram. The dashed lines show the effects of the 5.8 and 8.0 μm flux density limits. *Right*: SDSS color-magnitude diagram. Faint ($i \gtrsim 18$) point sources with $g - i \gtrsim 0.8$ are either high-redshift quasars or dust-reddened low-redshift quasars. In both panels, the contours/points are coded the same as in Fig. 6.

Figure 7 will produce the most complete AGN sample (including type 2 AGNs). However, such selection is not optimally efficient as a result of contamination by star-forming galaxies—particularly at faint MIR flux densities. The addition of optical colors and morphology can be used to achieve optimal efficiency with respect to type 1 AGNs at the expense of losing type 2 AGNs. A multidimensional MIR + optical Bayesian color-selection approach (Richards et al. 2004) that avoids any morphology bias may yield optimal completeness and efficiency for all AGN subclasses and will be the subject of future work.

4. THE OBSCURED QUASAR FRACTION

Since MIR emission from AGNs comes from larger scales and is thought to be more isotropic than optical/UV emission, the MIR is an ideal part of the spectrum to constrain the fraction of quasars that are obscured (within the context of the so-called unified model; Antonucci 1993). However, determining the obscured fraction requires careful comparison of the relative numbers of MIR- and optical/UV-detected AGNs, which is complicated by different MIR and optical/UV flux density limits and the shape of the mean SED (see § 5). Thus, in this section we make some comparisons between MIR-only selection and optical + MIR selection in terms of relative flux limits and examine the consequences for accurately determining the obscured quasar fraction.

Figure 9 shows mean quasar SEDs compared to various survey flux limits. The black solid and dashed lines are the (rest-frame) Elvis et al. (1994) mean radio-quiet and radio-loud SEDs, normalized to $i = 16.4$ (1 mJy). The colored dashes show the flux density limits for the *Spitzer* XFLS, *Spitzer* NOAO/Boötes (Jannuzi & Dey 1999; Eisenhardt et al. 2004), 2MASS, SDSS (imaging), SDSS ($z < 3$ quasar spectroscopy), and *GALEX* (Medium Imaging Survey [MIS]). The lighter gray lines show the radio-quiet SED at $z = 0.5$, 1.5, and 2.5 normalized to the Boötes field 8 μm flux limit. The dashed gray line shows the $z = 1.5$ SED reddened by SMC-like reddening with $E(B - V) = 0.45$.

Stern et al. (2005) estimate the fraction of obscured quasars missed by optical surveys by comparing their 8 μm source counts to a flux density limit of 76 μJy to the optical source counts of quasars at $R \sim 21$, assuming a spectral index of $\alpha_\nu = -0.73$. We revisit this analysis with two new considerations. First, we use the number counts of optically selected (g-band) quasars from Richards et al. (2005), which used SDSS imaging coupled with 2dF spectroscopy to determine the quasar luminosity function to $g \sim 21.5$. Second, rather than assuming a power-law SED, we use an empirical SED such as that from Elvis et al. (1994).

Stern et al. (2005) reported an obscured quasar fraction of $(275 - 65)/275 = 76\%$, where 275 is their candidate AGN density per square degree and 65 is the density of optically selected AGNs to $R = 21$ from Wolf et al. (2003). We find that a typical quasar with an 8 μm flux density of 76 μJy has a g-band magnitude of 21.5 ($r \sim 21.35$). Using the quasar luminosity function of Richards et al. (2005), we find an optically selected quasar density of 89 per square degree to $g = 21.5$. This density gives an upper limit to the obscured fraction of $(275 - 89)/275 = 68\%$.

However, since the quasar SED is *not* a power law between the optical and MIR, but rather exhibits some significant features (such as the 1 μm inflection), it is important to determine the g-band flux limit as a function of redshift.[16] The expected flux density of a type 1 quasar with an 8 μm flux density of 76 μJy can reach as faint as $g = 22.5$ depending on redshift and thus the optical counts will be underestimated. At that magnitude limit there are 170 optically selected quasars per square degree. We illustrate this issue in Figure 9, where one can see that at $z = 0.5$ the expected g and r flux densities of a typical quasar are much fainter (but still detectable by SDSS) than the optical-to-MIR flux ratio assumed by Stern et al. (2005) (*dotted line*). While the density of *luminous* quasars peaks at $z \sim 2.5$, where the Stern et al. (2005) extrapolation is roughly correct, X-ray surveys (e.g., Ueda et al. 2003) have shown that the density of lower luminosity AGNs peaks at lower redshifts and thus this effect is important.

If we instead use the mean SED that we will derive in § 5.2, the g-band magnitude for a 76 μJy source at 8 μm ranges between $g = 21.4$ and $g = 22.4$. The optically selected quasar densities for those magnitudes are 82 and 161 per square degree, respectively.

[16] It is probably equally as important to consider the obscured quasar fraction as a function of luminosity (Ueda et al. 2003; Hao et al. 2005), but that is beyond the scope of our analysis.

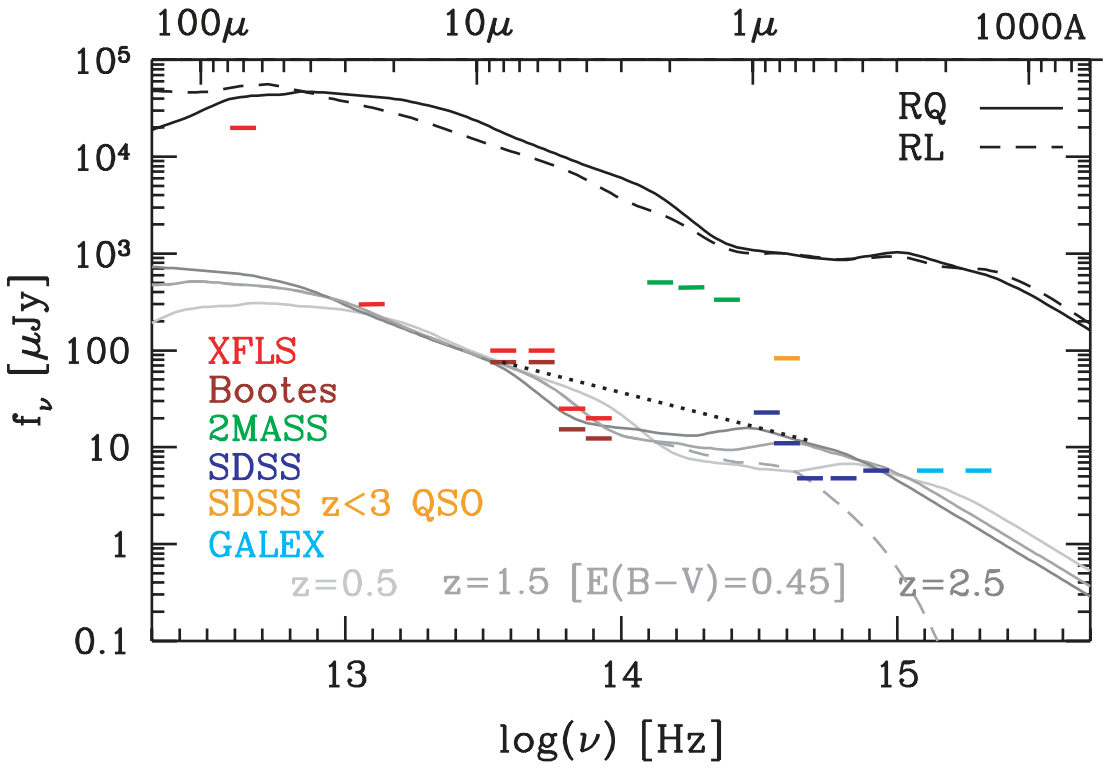

FIG. 9.—Mean quasar SEDs compared to various survey flux limits. The black solid and dashed lines are the $z = 0$ Elvis et al. (1994) mean radio-quiet and radio-loud SEDs, normalized to $i = 16.4$ (1 mJy). The colored dashes show the flux density limits for the *Spitzer* XFLS (*red*), *Spitzer* Boötes (*brown*; Stern et al. 2005), 2MASS (*green*), SDSS (imaging, *blue*), SDSS (low-z quasar spectroscopy, *orange*), and *GALEX* (*cyan*) surveys. The lighter gray lines show the radio-quiet SED at $z = 0.5$, 1.5, and 2.5 normalized to the Boötes field 8 μm flux limit [dashed gray line is $z = 1.5$ SMC-reddened by $E(B - V) = 0.25$]. The dotted line shows a spectral index of $\alpha_\nu = -0.73$ between 8 μm and the SDSS r band.

Using these numbers, we find that the fraction of obscured quasars has a lower limit in the ballpark of $(275 - 161)/275 = 41\%$. Finally, since the Stern et al. (2005) MIR-selected AGNs were selected to a rather faint MIR flux limit, then, as discussed above, some fraction of the AGN candidates may instead turn out to be normal star-forming galaxies and/or be contaminated by host galaxy light, which would also reduce the obscured quasar fraction.

Similar arguments can be made with regard to the obscured quasar fraction computed by Lacy et al. (2004). They found an obscured fraction of $(16/35) = 46\%$ by assuming that all 8 μm sources brighter than 1 mJy would be brighter than the SDSS's spectroscopic magnitude limit of $i = 19.1$. Using the Elvis et al. (1994) SED to determine the i magnitude for this 8 μm flux density as a function of redshift, we find that many IR-bright, low-redshift quasars will in fact be fainter than the SDSS spectroscopic limit. Again, this effect is largest at low redshift, but Lacy et al. (2004) find their obscured-AGN candidates are primarily low redshift. In principle, this would suggest that the obscured quasar fraction found by Lacy et al. (2004) is also an upper limit; however, in practice, their objects do appear to be bona fide obscured AGNs (Lacy et al. 2005a). This may be due in part to the relatively bright MIR flux limit imposed by those authors. Nevertheless, we caution that the shape of the SED can influence the expected MIR-to-optical ratio of quasars as a function of redshift.

Other work on obscured AGNs using *Spitzer* selection has typically suggested a large obscured quasar fraction. Martínez-Sansigre et al. (2005) use a combined radio and *Spitzer* 24 μm based selection in the XFLS to show that the ratio of obscured to type-1 quasars is in the range 1–3 : 1, but this estimate is dependent on a lack of evolution in the distribution of the ratio of radio to optical luminosities of quasars from low to high redshifts, as the majority of high-redshift quasars are expected to have much lower radio luminosities than probed by the radio survey of the XFLS by Condon et al. (2003). The deep, multiwavelength Great Observatories Origins Deep Survey (GOODS) finds a ratio of obscured to unobscured AGNs of $\sim$3 : 1 (Treister et al. 2004), but most of their AGNs are well below quasar luminosity and thus not directly comparable to the objects studied in this paper. It is also important to realize that mid-infrared selection may not find all obscured quasars, particularly at high redshift, where the IRAC bands are redshifted into the rest-frame near infrared, or in cases of objects viewed through very high ($A_V \sim 100$) extinctions, as expected for objects viewed through an obscuring torus edge-on to the line of sight. Improved modeling of the biases in mid-infrared selection of AGNs should remove much of this uncertainty.

In conclusion, MIR photometry from *Spitzer* promises to reveal the true fraction of obscured AGNs. However, full-characterization of the obscured fraction will require careful consideration of not only luminosity-dependent effects (which will require larger areas in order to recover enough bright quasars), but also redshift-dependent SED and host-galaxy effects.

5. SPECTRAL ENERGY DISTRIBUTIONS

5.1. *Introduction*

Accurate determination of quasar SEDs is crucial to our understanding of quasar physics. The strengths and shapes of the various components of a typical quasar SED have been used to determine the physical drivers in each frequency regime from the jets in the radio to the dusty torus in the mid- to far-IR, the accretion disk in the optical/UV/soft–X-ray, and the X-ray corona at the highest energies.

As the observed radiation from quasars is often reprocessed and re-emitted at wavelengths far different from the seed photons, knowing the overall SED is necessary for determining bolometric luminosities. In turn, bolometric luminosities are necessary for determining the so-called Eddington ratio ($L_{\rm bol}/L_{\rm Edd}$, or equivalently $L_{\rm bol}/M_{\rm BH}$), which serves as a measure of the accretion rate (relative to the Eddington accretion rate) of the system (e.g., Peterson 1997).

Despite a few recent additions/updates to Elvis et al. (1994 see, e.g., Polletta et al. 2000; Kuraszkiewicz et al. 2003; Risaliti & Elvis 2004), complete SEDs have been compiled for only a small number ($\lesssim$100) of quasars and the mean SED from Elvis et al. (1994) is arguably still the best description of the SED of quasars and is certainly the most commonly used. However, it is illuminating to recall the caveats given by the authors in the abstract of that paper: "We derive the mean energy distribution (MED) for radio-loud and radio-quiet objects and present the bolometric corrections derived from it. We note, however, that the dispersion about this mean is large ($\sim$1 decade for both the infrared and ultraviolet components when the MED is normalized at the near-infrared inflection). . .The existence of such a large dispersion indicates that the MED reflects on some of the properties of quasars and so should be used only with caution."

Furthermore, in addition to the SED diversity in their sample, it is well known that the sample used to construct this mean SED is not entirely representative: "Our primary selection criteria were (1) existing *Einstein* observations at good signal-to-noise ratio (to ensure good X-ray spectra) and (2) an optical magnitude bright enough to make an *IUE* spectrum obtainable." The first criterion means that the sample is biased toward X-ray bright quasars, and therefore typically objects with relatively high X-ray–to–optical flux ratios. Similarly, the second criterion biases the sample toward bluer quasars (see Jester et al. 2005).

Nevertheless, the mean SED from Elvis et al. (1994) has generally been found to be a robust template for typical type 1 quasars. However, given the diversity of the mean SED, the biases inherent to the sample, and the accuracy to which we would like to know the bolometric luminosity for a given quasar, it is important to improve our knowledge of the full SED of quasars to test how well this assumption holds and to investigate the full range of individual SEDs.

As there is often little overlap in the jargon and notation used to describe quasars in different bandpasses (e.g., blue/red/Å/mag in the optical, flat/steep/GHz/mJy in the radio, hard/soft/keV/cgs in the X-ray), it will aid our discussion to review quasar SEDs from a single multiwavelength point of view. Thus, in Figure 10 we show the mean radio-loud and radio-quiet quasar SEDs from Elvis et al. (1994) on a log-log plot of f_ν versus ν (*top*) and νf_ν versus ν (*bottom*). Here f_ν is given in ergs s^{-1} cm^{-2} Hz^{-1}, and the abscissa is given in log frequency, wavelength, energy, and temperature units. The normalization is such that the quasar has a continuum flux density of 0.08 mJy (AB = 19.1) at 2500 Å. Typical ranges of spectral indices within and between bands are shown; the spectral indices are given as energy indices where $f_\nu \propto \nu^\alpha$ such that α represents the *slope* (and is thus generally negative).

We wish to use Figure 10 to make a few points. First, there is considerable scatter in quasar SEDs in each energy regime and little is known about correlations in these variations *between* energy regimes. Second, the plots visually emphasize the point made above, which is that the Elvis et al. (1994) sample was quite X-ray bright. Finally, there is a strong need for better characterization of quasar SEDs in the near-IR through far-IR.

5.2. *Mean SEDs*

To explore the color and luminosity dependence of the quasar SED, we use the 259 SDSS quasars cataloged herein to construct new mean SEDs. The individual SEDs of these quasars are shown in the Appendix. For the sake of homogeneity, we have excluded the Hectospec-confirmed quasars from Papovich et al. (2005) as they were selected with different criteria than the SDSS-confirmed quasars.

These SEDs are constructed as follows. While all of our objects have 5 SDSS magnitudes and 4 *Spitzer* IRAC flux densities, many objects have no measurements in the 10 other bands that we catalog. Thus, we first attempt a form of "gap repair." For the *GALEX f* and *n* bands, *J*, *H*, and *K*, the *ISO* 15 μm band, and the *Spitzer* MIPS 24 and 70 μm bands, we replace missing values with those determined from normalizing the Elvis et al. (1994) SED in the next nearest bandpass for which we have data. For example, *n* is estimated from *u*, *J* from *z*, *K* from $S_{3.6}$, S_{15} from $S_{8.0}$, etc. For the radio-loud quasars we use the Elvis et al. (1994) mean radio-loud SED; the remaining quasars are repaired using the Elvis et al. (1994) mean radio-quiet SED.

Since the optical–to–X-ray flux ratio of the Elvis et al. (1994) SED is atypical, we do not perform the same sort of gap repair in the X-ray for those quasars that lack *ROSAT* detections. Instead, we use the $L_{\rm UV}$-$L_{\rm X}$ relationship that has been known since Avni & Tananbaum (1986) and has been well characterized by Strateva et al. (2005), and more recently by Steffen et al. (2006). This relationship parameterizes the relatively tight correlation between the 2500 Å and 2 keV brightness of quasars as a function of luminosity. Thus, we normalize the Elvis et al. (1994) SED to the average of the high-S/N (*gri*) SDSS measurements and determine the 2500 Å flux density for that normalization. Then we use the equations given by Strateva et al. (2005) to estimate the 2 keV flux density of each quasar. We then assume a flat (in νf_ν space, which has $\alpha_x = -1.0$) spectrum between 0.1 and 10 keV, roughly consistent with Reeves & Turner (2000) and George et al. (2000). Finally, as there are only 8 radio-loud quasars in our sample and wavelengths shortward of $\sim$100 μm are energetically unimportant, we ignore any missing radio information (although all the objects have upper limits).

In addition to gap repair, it is necessary to correct for host galaxy contamination, which can have a significant effect in many of the bandpasses that we consider. Lacking the data to measure the host galaxies of our sources, we must estimate their contribution. Such estimates of the contribution of host galaxy light to the SEDs can be made by applying simple scaling relationships among host bulge luminosity, bulge mass, black hole mass, and Eddington luminosity (e.g., Dunlop et al. 2003; Vanden Berk et al. 2006). The well-known correlation between central black hole mass and both bulge mass and luminosity (e.g., Ferrarese 2002) implies that quasars accreting at near their Eddington limits must have host bulge masses, and therefore luminosities, large enough to harbor the inferred black hole. We have used the quasar luminosity versus host luminosity relationship at optical frequencies, described by Vanden Berk et al. (2006), to estimate the relative host galaxy contribution, assuming that the quasars are emitting at their Eddington limits.

We specifically convert the M_i relationship used by Vanden Berk et al. (2006) to a luminosity and determine the host galaxy luminosity as

$$\log(L_{\rm Host}) = 0.87\log(L_{\rm AGN}) + 2.887 - \log(L_{\rm Bol}/L_{\rm Edd}), \quad (1)$$

where the host galaxy and AGN luminosities are specific luminosities at 6156 Å (the effective wavelength of the SDSS *r* band)

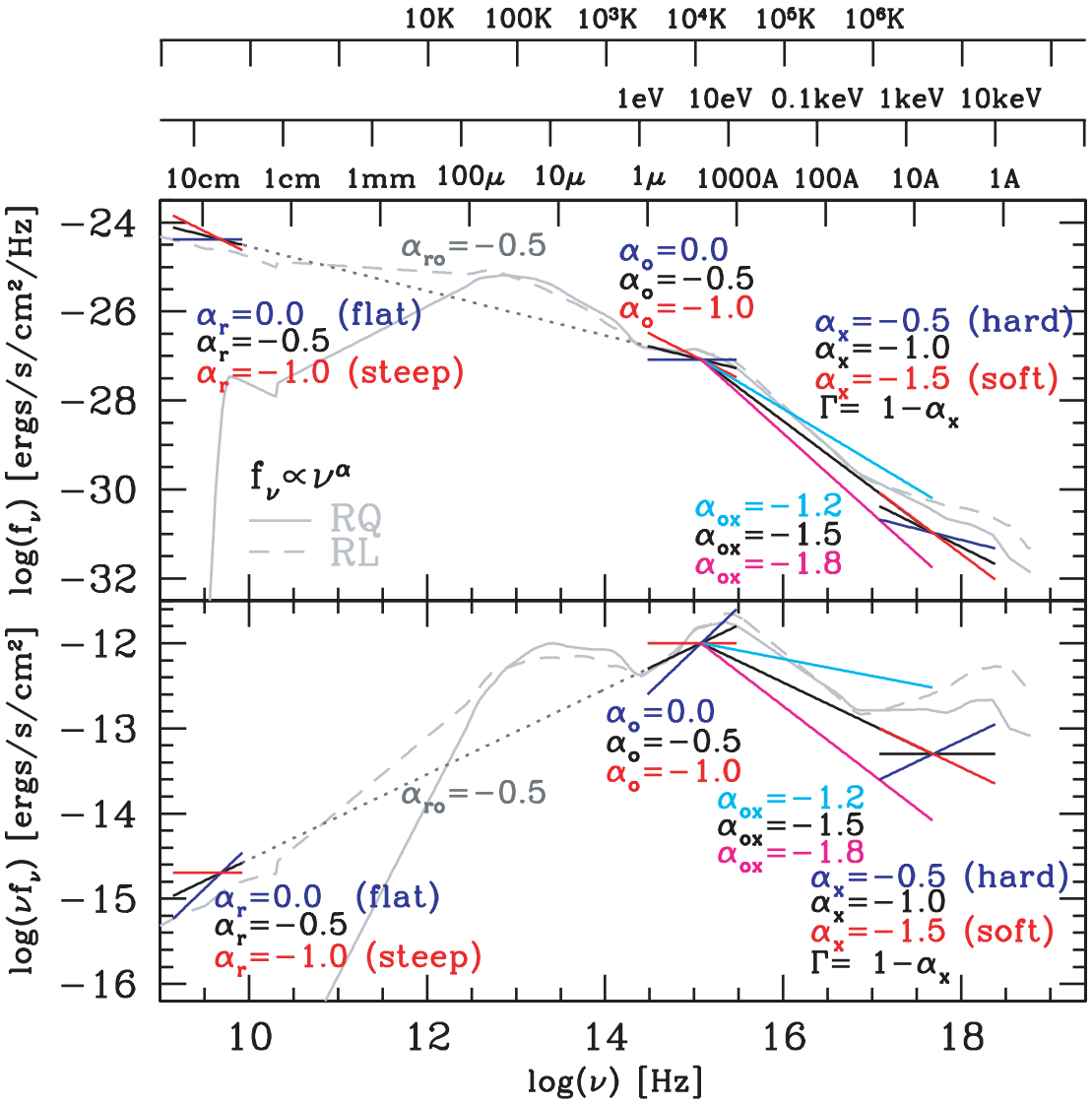

FIG. 10.—Quasar SED diagnostic plot. Shown in gray are the Elvis et al. (1994) radio-quiet (*solid*) and radio-loud (*dashed*) mean SEDs. The colored lines indicate typical spectral indices in the radio, optical, and X-ray using the same sign convention. Also shown is the typical radio-to-optical spectral index for radio-loud quasars and the range of optical–to–X-ray spectral indices. Studies in different bands tend to use different sign conventions for spectral indices and jargon to describe them (e.g., steep/red/soft). The top panel shows f_ν, while the bottom panel shows νf_ν. The x-axis is labeled as log (ν) (*bottom*), and wavelength, energy, and temperature (*top*).

and we have taken $L_{\rm Bol}/L_{\rm Edd}$ to be unity. This synthesis of multiple scaling relations will have considerable scatter, and many, if not most, AGNs will be accreting at much lower Eddington ratios. However, we have found that a value of $(L_{\rm Bol}/L_{\rm Edd}) = 1$ works well and has the nice feature that it represents the *minimum* host galaxy contribution that *must* be accounted for (smaller ratios implying relatively more luminous hosts).

This process sets the relative scaling of the host galaxy in the r bandpass. To actually subtract the host galaxy contribution at all wavelengths, we use the elliptical galaxy template of Fioc & Rocca-Volmerange (1997) scaled according to the prescription above. We ignore the differences between spiral and elliptical hosts as the host galaxy contribution is small where these differences matter most. Since equation (1) requires knowing $L_{\rm AGN}$ and we instead know $L_{\rm Tot} = L_{\rm AGN} + L_{\rm Host}$, we use an iterative process to determine $L_{\rm Host}$. In particular, we first assume that $L_{\rm AGN} = L_{\rm Tot}$ (in the r band) and compute $L_{\rm Host}$. We then subtract the host contribution from the total luminosity to give a more accurate estimate of $L_{\rm AGN}$, from which we compute a revised value of $L_{\rm Host}$.

Using the relative scaling of the elliptical galaxy (host) template with respect to the observed quasar (plus host) SED, we can determine the fractional contribution of the host galaxy at any other wavelength. To assess the importance of the host galaxy correction where it matters most, we determine the ratio of host galaxy to total luminosity at 1.6 μm in the rest frame, where the elliptical template spectrum has its peak. At 1.6 μm, we find that the host galaxy contributes between 30% and 38% of the total observed 1.6 μm luminosity. This fraction approaches unity for $(L_{\rm Bol}/L_{\rm Edd}) = 1/3$, which suggests that our quasars are generally close to Eddington (within a factor of $\sim$3) and/or that equation (1) does not perfectly parameterize the relationship between AGN luminosity $(L_{\rm Bol}/L_{\rm Edd})$ and the host galaxy luminosity.

In practice, we have removed the host galaxy contribution before applying the above gap-repair process since the Elvis et al. (1994) template has already been corrected for the host galaxy contribution. Furthermore, we stress that, at $z = 1.5$, 1.6 μm in the rest-frame corresponds to 4 μm in the observed frame; thus, MIR-selected samples are strongly affected by host galaxy contamination.

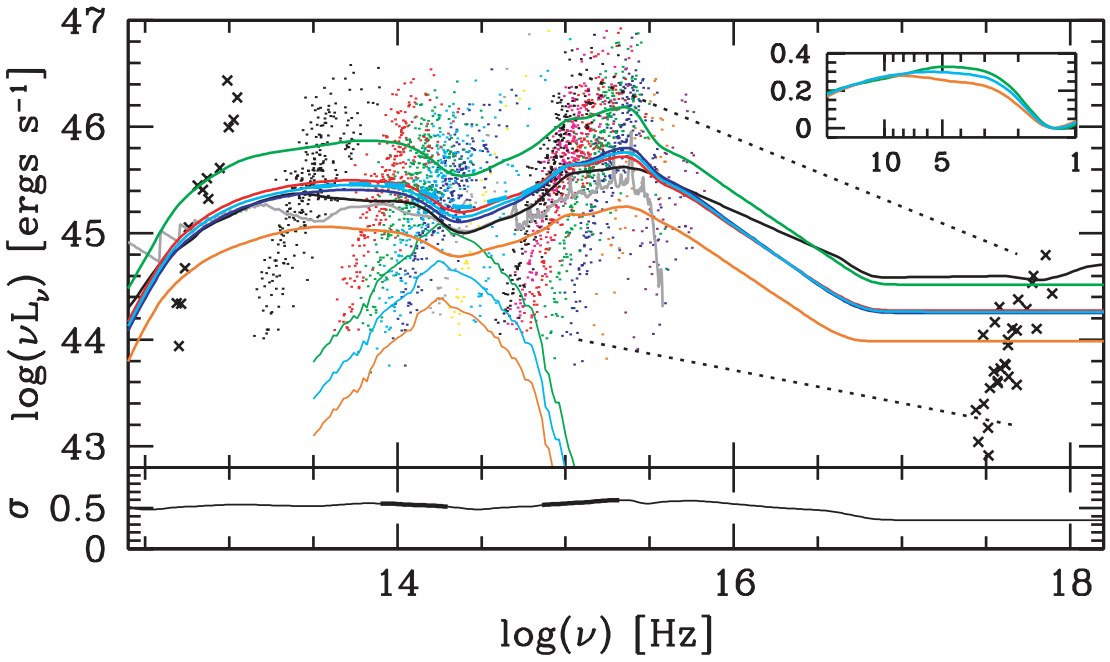

FIG. 11.—Mean quasar SEDs and the data used to construct them. The points show the data; the lines show the mean SEDs. From left to right: *black crosses*, MIPS70; *black points*, MIPS24/ISO15; *red points*, $S_{8.0}$; *green points*, $S_{5.8}$; *cyan points*, $S_{4.5}$; *blue points*, $S_{3.6}$; *gray points*, *K*; *yellow points*, *H*; *cyan points*, *J*; *black points*, *z*; *magenta points*, *i*; *red points*, *r*; *green points*, *g*; *blue points*, *u*; *orange points*, *n*; *purple points*, *f*; *black crosses*, X-ray. The dotted lines show the range of α_{ox} with luminosity for the luminosity extremes of our sample (Strateva et al. 2005). From top to bottom (at 10^{14} Hz) the thick solid lines are color coded as follows: *green*, optically luminous SDSS quasars; *red*, optically red SDSS quasars; *cyan*, all SDSS quasars; *blue*, optically blue SDSS quasars; *black*, Elvis et al. (1994) radio-quiet mean SED; *gray*, Hatziminaoglou et al. (2005) mean SED (normalized to Elvis et al. 1994 at 1 μm); *orange*, optically dim SDSS quasars. The near-IR luminous/dim composites are nearly identical to the optical composites. The thin green, cyan, and orange curves show the host galaxy contribution assuming $(L_{Bol}/L_{Edd}) = 1$ (see eq. [1]) for the elliptical galaxy composite spectrum of Fioc & Rocca-Volmerange (1997). The dashed cyan curve shows the effect of ignoring the host contribution. The inset at the upper right zooms in on the MIR region of the spectrum. The three curves are normalized at 1.3 μm, and the *y*-axis shows relative luminosity (νL_ν), while the *x*-axis is in microns. The bottom panel shows the 1 σ error array (dex) for our overall mean SED. Those frequencies where over 100 quasars contribute to the mean SED are shown as thicker line segments and are relatively unaffected by the gap-repair process.

As we wish to investigate the mean properties of quasars as a function of luminosity, color, etc., we next combine the corrected individual SEDs and construct a number of different mean SEDs. We first convert the flux densities of each individual object to luminosities in our adopted cosmology and shift the bandpasses to the rest frame. We then create a grid of points separated by 0.02 in log frequency and linearly interpolate between the 19 rest-frame effective frequencies that are populated by our gap-repaired photometry.

The resulting geometric mean SEDs are shown as colored curves in Figure 11. The individual data points for our quasars are also shown, color-coded by band. The mean of all our objects is shown in cyan with the dashed cyan line showing the effect of ignoring the host contribution (where the host contribution is indicated by the thin cyan line that peaks near $10^{14.3}$ Hz). The bottom panel shows the 1 σ standard deviation for the overall mean SED, with thicker line segments indicating the regions where the SED is least affected by gap repair. We have further constructed mean SEDs for the optically luminous/dim and optically blue/red halves of the population. The median values used to split the distributions are optical: $\log(L) = 46.02$; IR: $\log(L) = 46.04$; color: $\Delta(g - i) = -0.04$; where extremely red quasars having $\Delta(g - i) > 0.3$ were excluded from the construction of all the composite SEDs (19 quasars in all). These mean SEDs are given in tabular form in Table 3.

Since the quasar sample is not completely homogeneous (e.g., $z > 3$ quasars were generally selected 1 mag deeper than $z < 3$ quasars) we have not tabulated the confidence intervals (as in Fig. 11 of Elvis et al. 1994). However, the standard deviation of the overall mean and the luminosity- and color-subdivided mean SEDs give the reader an idea of the range of SED shapes. As the sample size increases with additional data, particularly from *Spitzer*, it will be possible to make further subdivisions (e.g., luminous blue quasars, as a function of mass, etc.) to better explore the range of SEDs.

One of the primary purposes of constructing these mean SEDs as a function of various quasar properties is to see how the MIR part of the SED changes with these properties. Interestingly,

TABLE 3
MEAN QUASAR SEDS

log Hz	All	σ_{All}	Blue	Red	Opt. Lum.	Opt. Dim.	IR Lum.	IR Dim.
12.50.....	44.43	0.49	44.39	44.47	44.76	44.12	44.82	44.10
12.52.....	44.49	0.49	44.44	44.53	44.81	44.18	44.87	44.16
12.54.....	44.54	0.49	44.50	44.58	44.87	44.23	44.93	44.22
12.56.....	44.59	0.49	44.55	44.64	44.93	44.28	44.98	44.27
12.58.....	44.65	0.49	44.60	44.69	44.98	44.33	45.04	44.32
12.60.....	44.70	0.50	44.65	44.74	45.03	44.38	45.09	44.36
12.62.....	44.74	0.50	44.70	44.78	45.09	44.42	45.15	44.40
12.64.....	44.79	0.50	44.74	44.83	45.14	44.45	45.20	44.44
12.66.....	44.83	0.51	44.78	44.87	45.19	44.49	45.25	44.48
12.68.....	44.87	0.51	44.82	44.91	45.23	44.52	45.29	44.51

NOTES.—All of the SEDs are taken to have $\alpha_x = -1.0$ beyond 10^{17} Hz and thus have constant luminosity beyond this value. Units are $\log(\text{ergs s}^{-1})$. Table 3 is available in its entirety in the electronic edition of the *Astrophysical Journal Supplement*. A portion is shown here for guidance regarding its form and content.

we find that the *shape* of the MIR part of the SED is very similar for optically blue and optically red quasars. However, there are significant differences between the most and least optically luminous quasars in our sample. The inset of Figure 11 shows that the optically luminous quasars are much brighter in the 4 μm region than the least optically luminous quasars. These differences have the potential for being diagnostics for the physical parameters (such as orientation and dust temperature) that go into AGN dust models (e.g., Nenkova et al. 2002; Dullemond & van Bemmel 2005). For example, the excess 2–8 μm emission in the most luminous quasars with respect to the least luminous quasars is roughly consistent with the expected effects of luminosity in a clumpy torus model (e.g., Nenkova et al. 2002; Elitzur et al. 2003). In such models, lines of sight that observe the illuminated face of optically thick clouds are relatively brighter between 2 and 20 μm. Since the fraction of such lines of sight increases with the torus opening angle (with respect to disk normal) and more luminous quasars are thought to have larger torus opening angles (more specifically, lower obscured fractions), it may not be surprising to find that more optically luminous quasars are relatively brighter at $\sim$4 μm. *Spitzer* IRS spectra are needed to determine if these differences are truly continuum features or if perhaps they are due to emission lines (e.g., Paα and Brα, which are at 4.05 and 1.88 μm, respectively).

6. BOLOMETRIC LUMINOSITIES AND ACCRETION RATES

The determinations of quasar physical parameters such as bolometric luminosity, black hole mass, and accretion rate have been revolutionized by two bodies of work from the past decade or so. The first is the construction of mean quasar SEDs such as by Elvis et al. (1994), which allow one to estimate the bolometric luminosity of a quasar from a monochromatic luminosity and the assumption of a standard SED. The other is the reverberation mapping work led by Wandel et al. (1999) and Kaspi et al. (2000) (see also Kaspi et al. 2005), which allows one to infer a characteristic radius for the broad emission line region from the bolometric luminosity of the object and thus to relate the widths of emission lines to the mass of the central black hole. With these two pieces of information, we can derive a third (related) quasar property—the Eddington ratio ($L_{\rm Bol}/L_{\rm Edd}$, or equivalently $L_{\rm bol}/M_{\rm BH}$), which is an indicator of the accretion rate (relative to the Eddington accretion rate).

Our primary purpose for constructing these new SEDs is to investigate how the bolometric luminosities and accretion rates derived from them differ from those determined by assuming the mean SED from Elvis et al. (1994). As discussed above, the biases inherent to the sample of objects used by Elvis et al. (1994) in addition to these authors' warnings of the diversity of individual SEDs, coupled with the use of their mean SED as a single universal template, is what motivates this investigation.

Figure 12 thus shows the frequency-dependent bolometric corrections (where the bolometric luminosity is taken to be the 100 μm to 10 keV integrated luminosity) derived from each of the mean SEDs shown in Figure 11. The bolometric correction from 5100 Å for the Elvis et al. (1994) radio-quiet SED is 12.17.[17] As our SDSS-selected sample is less biased than that of Elvis et al. (1994), it should provide a more robust template for type 1 quasars, and further, the larger sample of objects allows us

[17] A 5100 Å bolometric correction value of between 8 and 10 is more commonly used in the literature (e.g., Kaspi et al. 2000).

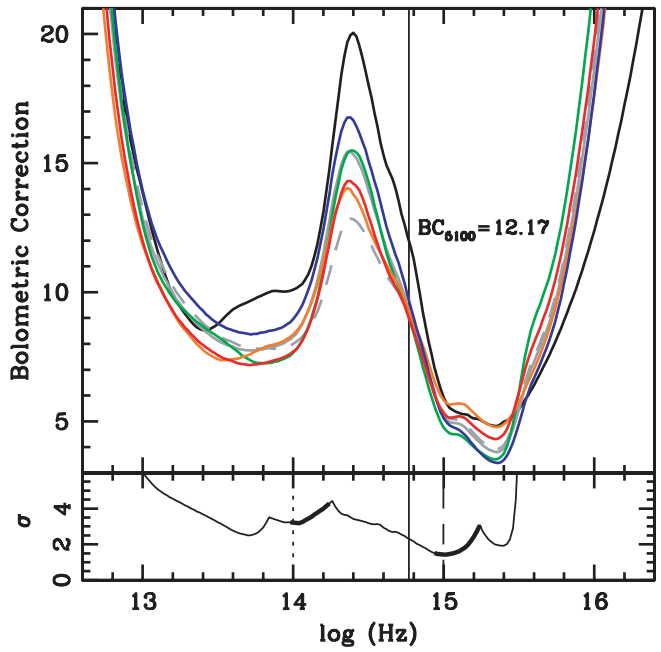

FIG. 12.—Bolometric corrections as a function of frequency for the SEDs in Fig. 11. The color coding is the same as for the previous figure (except that the full SDSS-DR3 mean quasar SED is now shown in gray instead of cyan). The dashed gray curve shows the full-sample mean SED without correction for the host galaxy contribution. The bolometric correction from 5100 Å for the Elvis et al. (1994) radio-quiet SED is 12.17 (*thin solid line*). As in Fig. 11, the bottom panel shows the 1 σ error in the bolometric correction derived from the overall mean SED with the most robust parts of the SED shown by thicker line segments. The kinks in the error spectrum attest to the importance of considering the range of quasar SEDs by demonstrating the homogenizing effects of assuming a single mean SED in our gap repair process. The vertical lines in the bottom panel indicate the frequencies that are compared in Fig. 13.

to consider the quasar SED not only in the mean, but as a function of various quasar properties. We see that in the MIR in particular, it is important to consider the range of SEDs possible when converting a monochromatic MIR luminosity to a bolometric luminosity. Curiously, in the rest-frame optical, where bolometric corrections are normally determined (usually at 5100 Å), the differences in the composite SEDs are relatively small. In fact, in terms of fractional error ($\sigma_{\rm BC}$/BC), the 5100 Å value appears to a robust choice of wavelength for converting monochromatic luminosity to bolometric luminosity. It seems likely that the minimum in this region results from this region being a relative minimum in the combination of host galaxy contamination in the near-IR and dust extinction in the UV.

Looking at the mean SEDs understates the differences for individual objects, however. Figure 13 shows a histogram of the individual bolometric corrections for each quasar in our sample at the frequencies shown in the bottom panel of Figure 12. The mean *B*-band bolometric correction from Elvis et al. (1994) was 11.8 with a range of [5.5, 24.7]; our mean and standard deviation at 5100 Å are 10.3 $\pm$ 2.1. The individual bolometric corrections (and $L_{\rm bol}$) are also given in Table 1. In this figure, we see that the average quasar has its bolometric luminosity overestimated by $\sim$17% when using the Elvis et al. (1994) SED at 5100 Å and that objects can have their bolometric luminosities misestimated by up to 50%. These errors propagate directly to errors in the accretion rate. Figures 12 and 13 demonstrate that the smallest bolometric corrections and errors are found at optical wavelengths. However, the fractional error has a broad minimum including

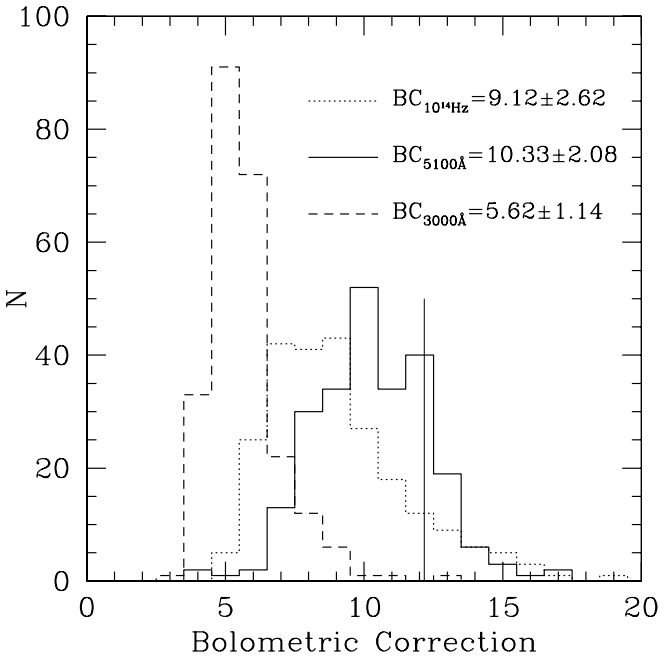

FIG. 13.—Histogram of bolometric corrections (from the indicated wavelength/frequency to 100 μm–10 keV) for our sample. Likely dust-reddened quasars [those having $\Delta(g - i) > 0.3$] have been excluded. The solid histogram shows the bolometric correction from 5100 Å with the vertical line indicating the value from Elvis et al. (1994). The 5100 Å bolometric correction (and thus the accretion rate relative to Eddington) is overestimated by 17% on the average if the Elvis et al. (1994) RQ SED is assumed to apply to all quasars. The dotted and dashed lines show the bolometric corrections at 10^{14} Hz and 3000 Å respectively (see Fig. 12). Individual objects can have their bolometric corrections misestimated by as much as 50% when assuming a single mean SED.

5100 Å, which a posteriori justifies the standard use of this wavelength for computing bolometric luminosities. Unfortunately, we find no strong trends between the bolometric correction and color or luminosity. Thus, it is difficult to know when to apply anything other than the mean bolometric correction. Clearly, if we are ever to understand the accretion rate distribution of quasars, we must either measure the bolometric luminosity directly or determine bolometric corrections to an accuracy better than that which is afforded by assuming the mean SED.

A final caveat is that it must be understood that bolometric corrections and bolometric luminosities determined by summing up all of the observed flux are really *line-of-sight* values that assume that quasars emit isotropically, when, in fact, we know that this is not the case. For example, the same quasar seen both face-on and edge-on need not yield SEDs that sum to the same bolometric luminosity; all of the energy must eventually escape, but not necessarily equally along all lines of sight. Thus, in Table 1, in addition to the bolometric luminosity, we also compute the integrated optical and IR luminosities. The integrated IR luminosity may be a more appropriate luminosity measure if the IR emission is largely isotropic (although even at 30 μm, IR emission is expected to be highly anisotropic; van Bemmel & Dullemond 2003). Alternatively, one might prefer to use the integrated optical/UV luminosity since nearly all photons emitted at other wavelengths by AGNs are reprocessed optical/UV/soft–X-ray seed photons. In either case, until we fully understand the SEDs of quasars as a function of observed quasar properties, and we can associate those properties with accurate geometrical models, bolometric luminosity and accretion rate determination will continue to have a significant degree of uncertainty.

7. CONCLUSIONS

We have compiled a sample of 259 SDSS type 1 quasars with four-band *Spitzer* IRAC detections. These data are supplemented with multiwavelength data spanning the radio to X-ray where available. We have shown that, while MIR-only selection of AGNs is indeed very efficient, adding optical morphology and color information allows for even more efficient selection of type 1 quasars. This multiwavelength data set was used to construct new mean SEDs of quasars as a function of color and luminosity, such as are needed to span the diversity of quasars in terms of computing accurate bolometric luminosities and accretion rates. It was shown that computing a bolometric luminosity from an optical luminosity by assuming a single mean quasar SED can lead to errors as large as 50%, which translate directly to an error in the presumed accretion rate. However, more data are needed to determine when and if it is appropriate to use template SEDs other than the mean to determine more accurate bolometric luminosities. Finally, judicious use of the knowledge of the mean quasar SED makes it possible to estimate the fraction of AGNs that are obscured in the optical by considering the redshift dependence of the relative flux limits between the optical and MIR and shows that the obscured fraction is lower than has been estimated previously.

Funding for the SDSS and SDSS-II has been provided by the Alfred P. Sloan Foundation, the Participating Institutions, the National Science Foundation, the US Department of Energy, the National Aeronautics and Space Administration, the Japanese Monbukagakusho, the Max Planck Society, and the Higher Education Funding Council for England. The SDSS Web site is http://www.sdss.org/. The SDSS is managed by the Astrophysical Research Consortium for the Participating Institutions. The Participating Institutions are the American Museum of Natural History, Astrophysical Institute Potsdam, University of Basel, Cambridge University, Case Western Reserve University, University of Chicago, Drexel University, Fermilab, the Institute for Advanced Study, the Japan Participation Group, Johns Hopkins University, the Joint Institute for Nuclear Astrophysics, the Kavli Institute for Particle Astrophysics and Cosmology, the Korean Scientist Group, the Chinese Academy of Sciences (LAMOST), Los Alamos National Laboratory, the Max-Planck-Institute for Astronomy (MPA), the Max-Planck-Institute for Astrophysics (MPIA), New Mexico State University, Ohio State University, University of Pittsburgh, University of Portsmouth, Princeton University, the United States Naval Observatory, and the University of Washington. This work is based on observations made with the *Spitzer Space Telescope*, operated by the Jet Propulsion Laboratory (JPL), California Institute of Technology, under contract with NASA. Support was provided by NASA through JPL. G. T. R. further acknowledges support from a Gordon and Betty Moore Fellowship in data intensive sciences. X. F. and M. V. acknowledge support from NSF grant AST-0307384. We thank an anonymous referee, especially for helping with figure presentation and also Eilat Glikman for making her IR quasar composite spectrum available in advance of publication.

APPENDIX

Figure 14 presents the individual SEDs of each of the 259 quasars in our sample. The plots are ordered by redshift to match Tables 1 and 2. The individual broadband data points are shown by gray squares. These are the observed values; host galaxy contamination has *not* been removed. The SDSS spectra are shown as solid black lines (smoothed by a 19 pixel boxcar). The SDSS spectra have been scaled by the difference between the *g*-, *r*-, and *i*-band PSF and fiber (3.″0) magnitudes to account for light losses due to the finite size of the optical fibers. The Elvis et al. (1994) radio-quiet mean SED is shown by the gray curves and is normalized to the 3.6 μm data point of each quasar.

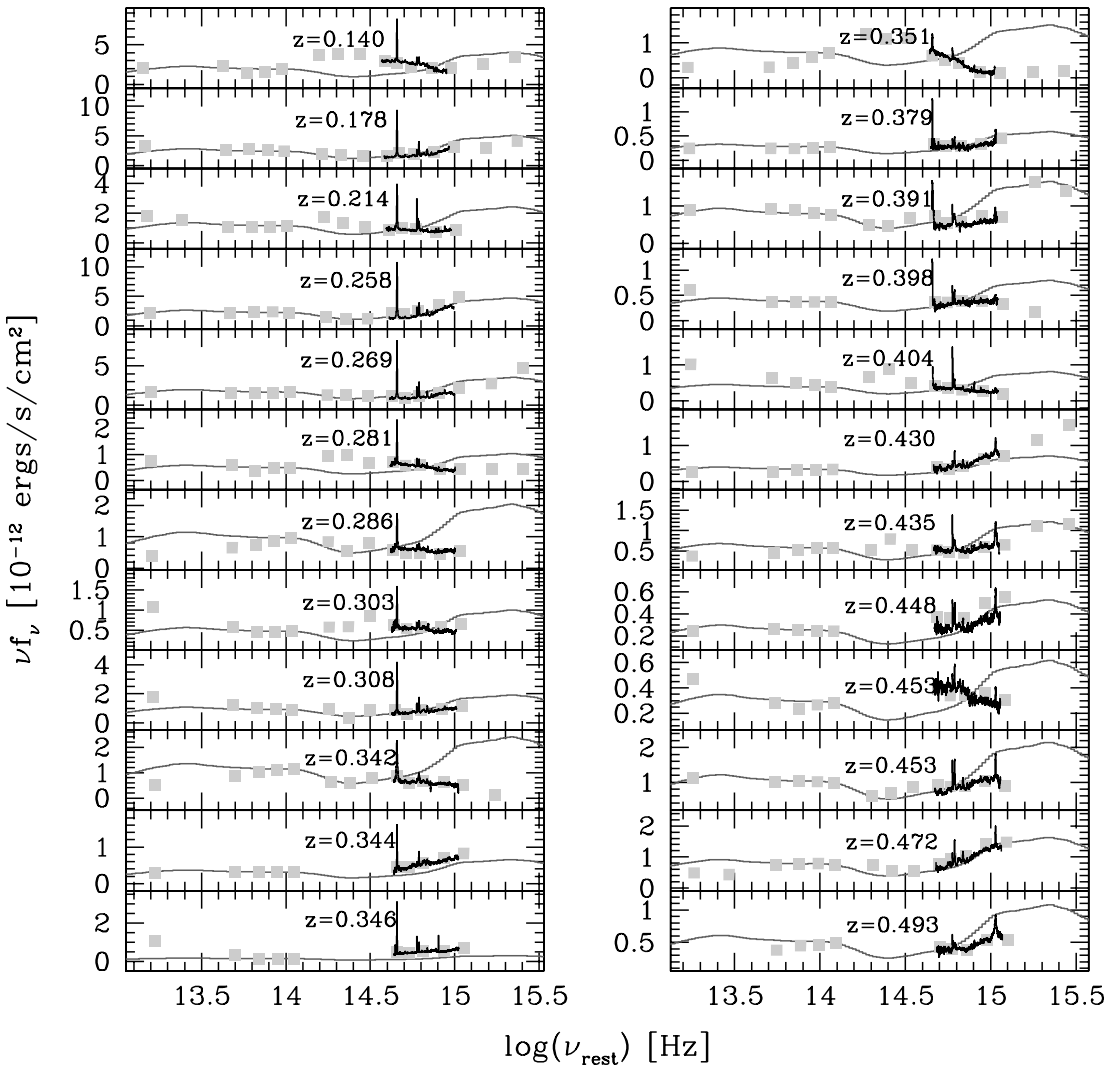

FIG. 14.—Individual mid-IR through UV SEDs for the quasars in our sample. The objects are ordered and labeled by redshift to correspond with the entries in Tables 1 and 2. The black curve shows the SDSS spectrum (scaled by the average magnitude difference between the *g*-, *r*-, and *i*-band point spread function and fiber magnitudes to correct for fiber losses). The gray curve shows the Elvis et al. (1994) mean radio-quiet SED (normalized to the 3.6 μm point). The lighter gray symbols represent the available broadband photometric measurements for these objects from *Spitzer* MIPS, *ISO*, *Spitzer* IRAC, 2MASS, SDSS, and *GALEX*. No host galaxy correction has been applied.

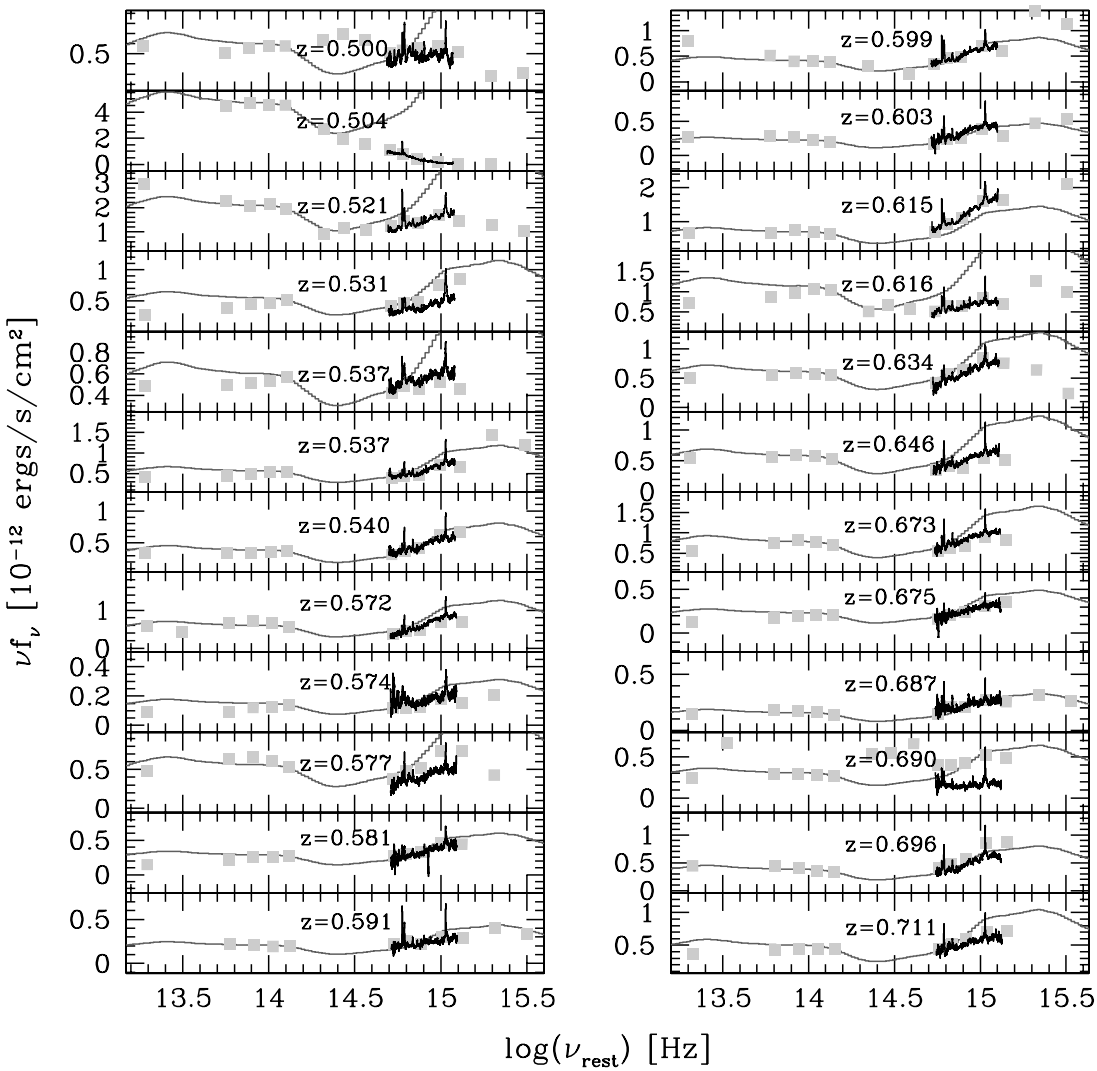

FIG. 14.—*Continued*

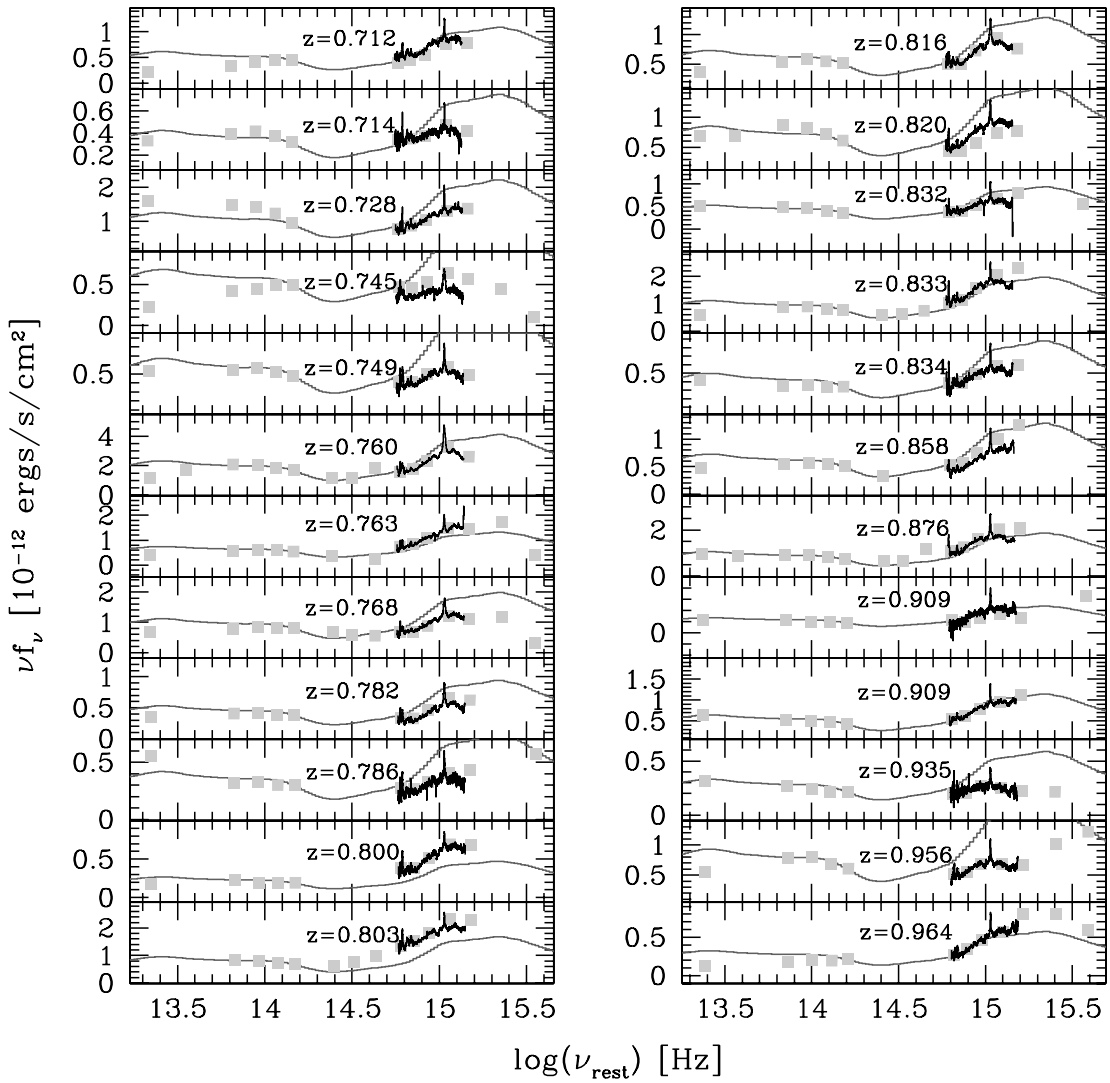

FIG. 14.—*Continued*

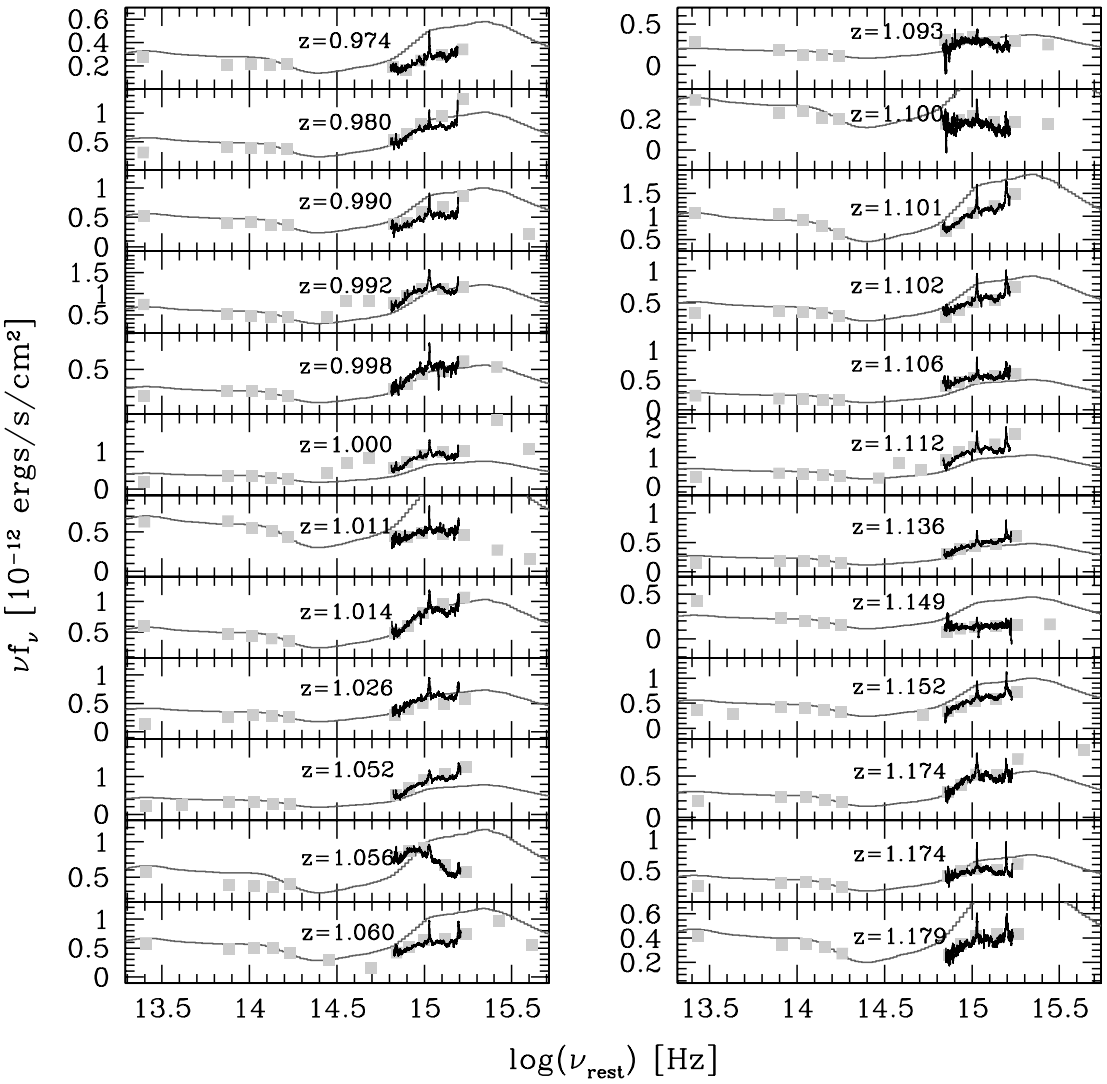

FIG. 14.—*Continued*

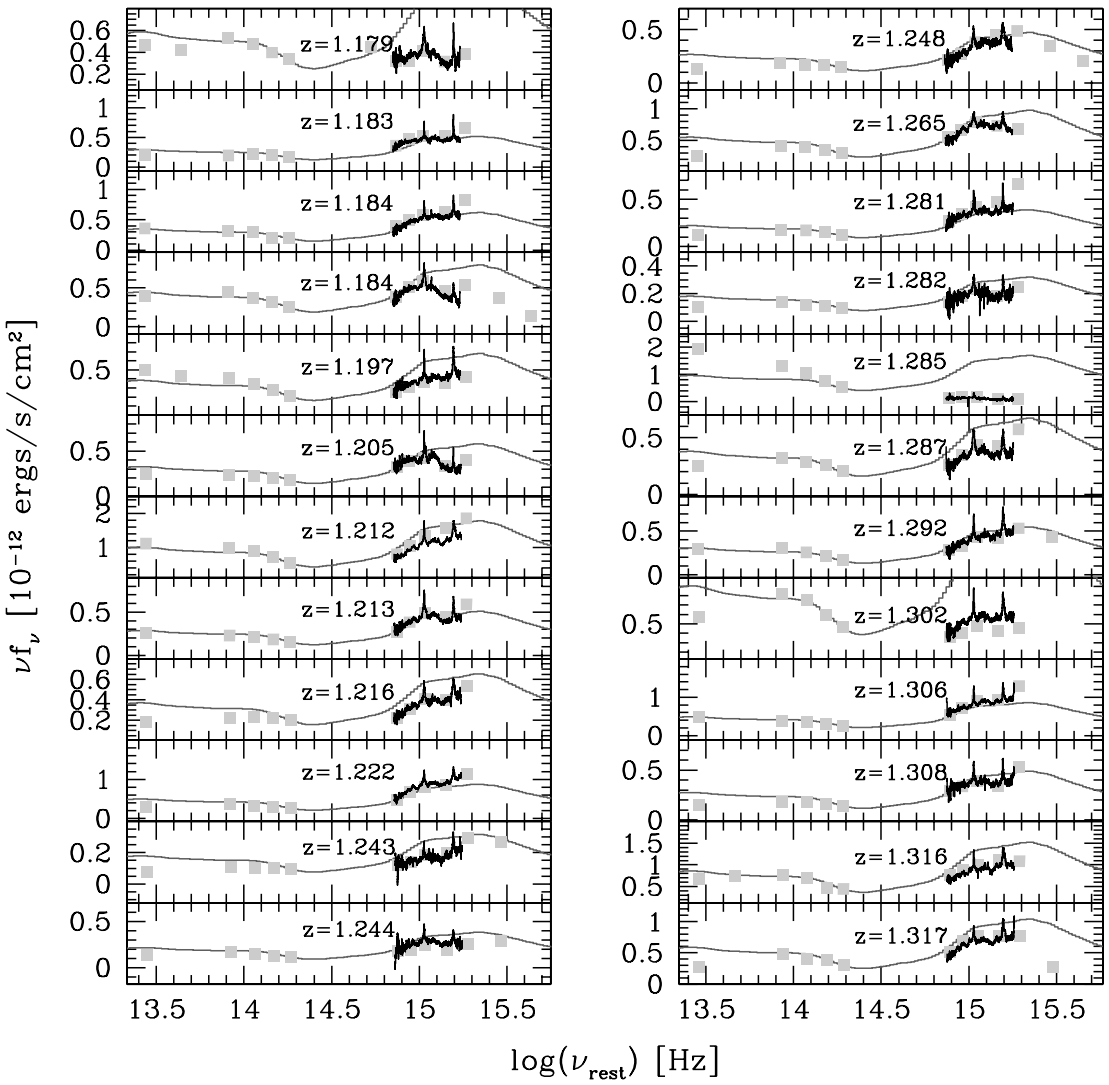

FIG. 14.—*Continued*

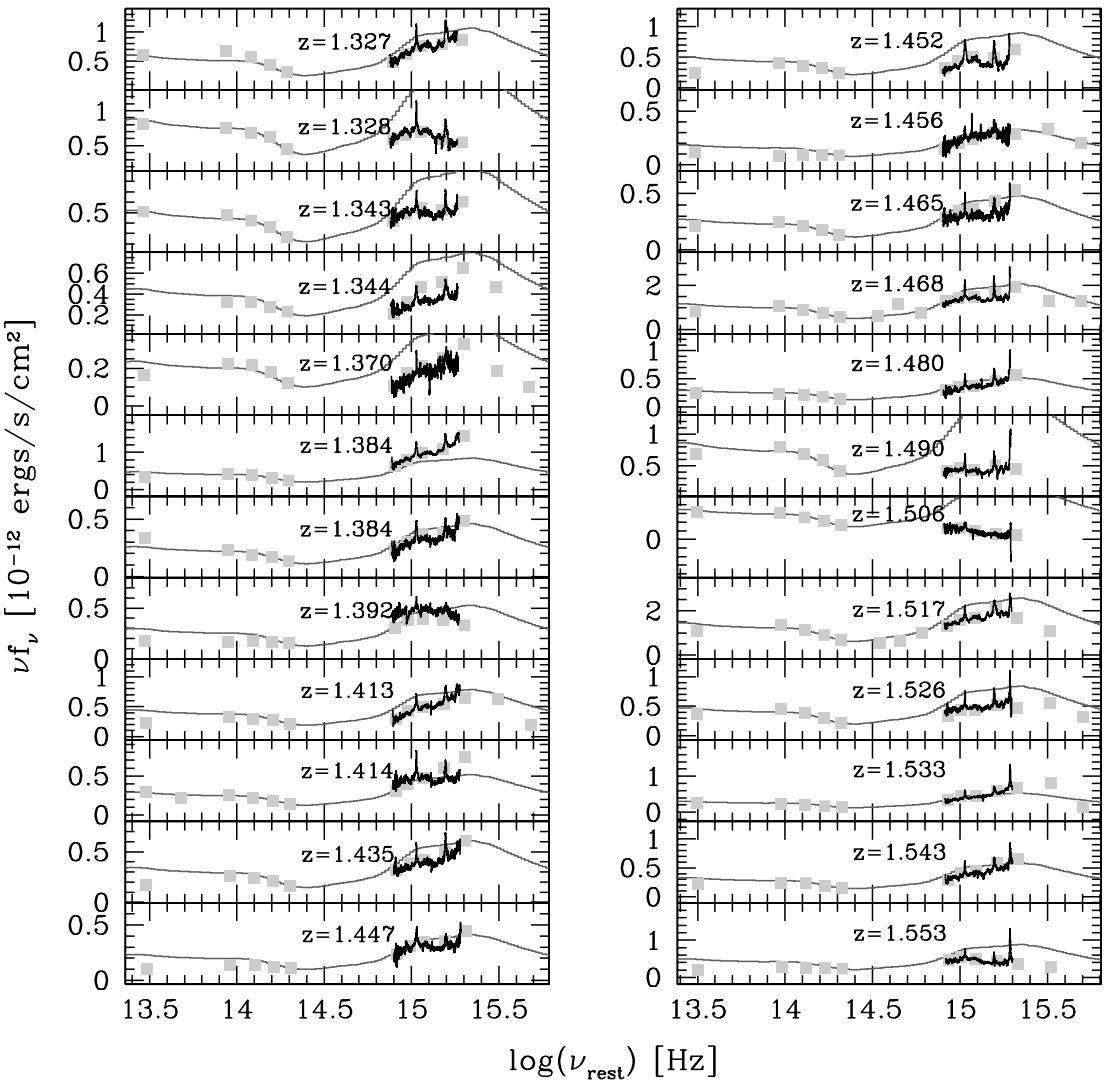

FIG. 14.—*Continued*

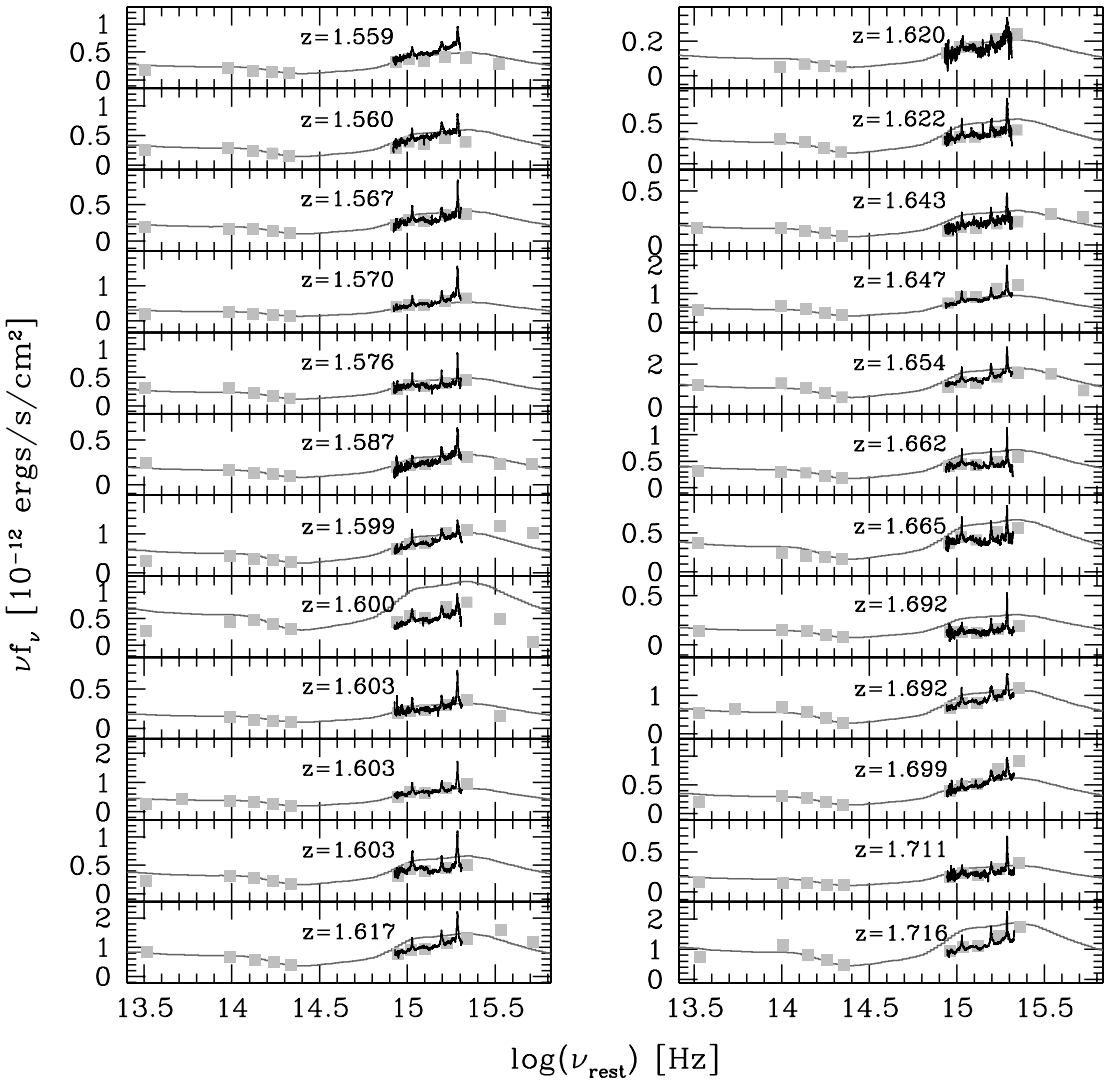

FIG. 14.—*Continued*

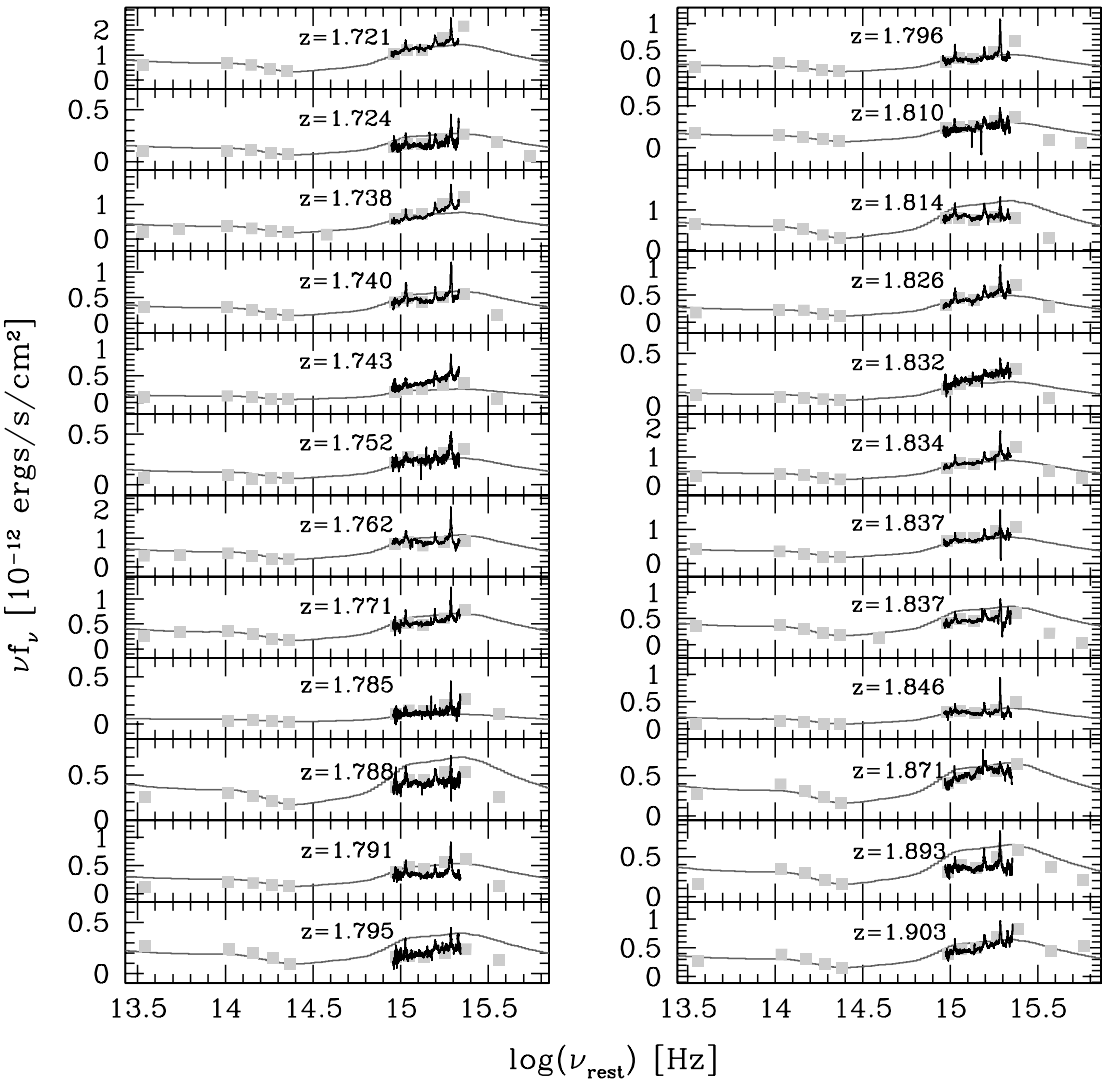

FIG. 14.—*Continued*

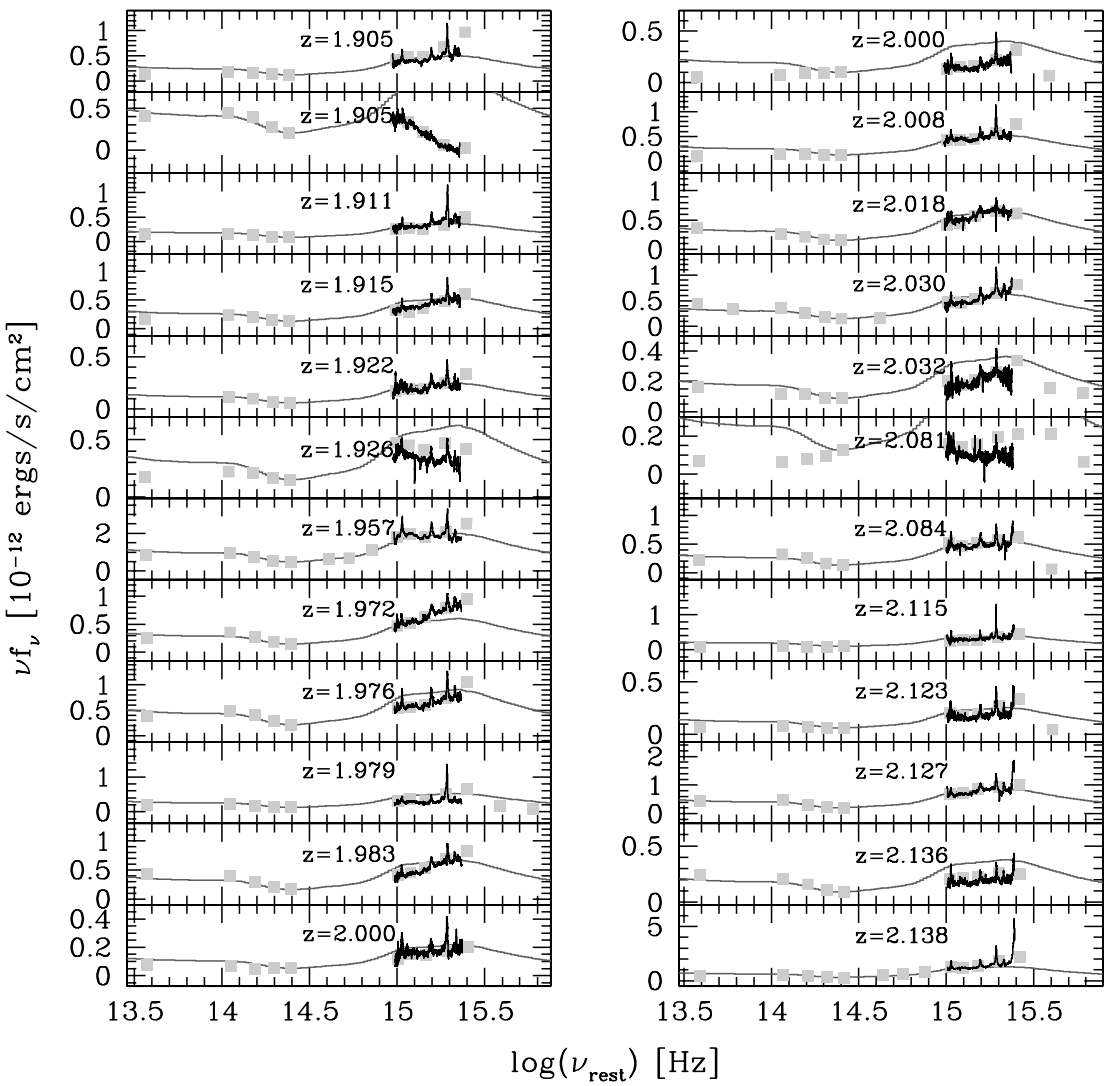

FIG. 14.—*Continued*

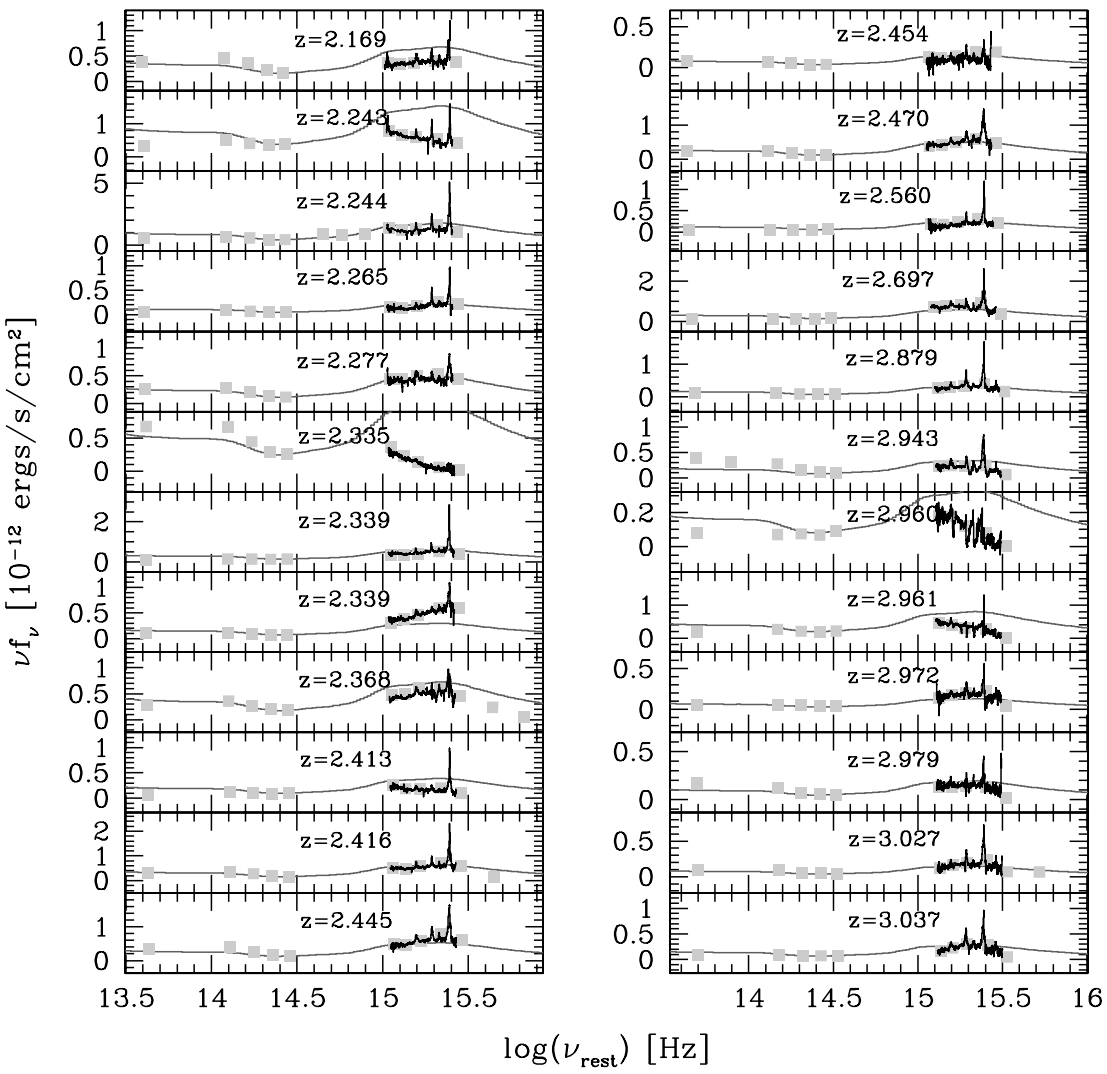

FIG. 14.—*Continued*

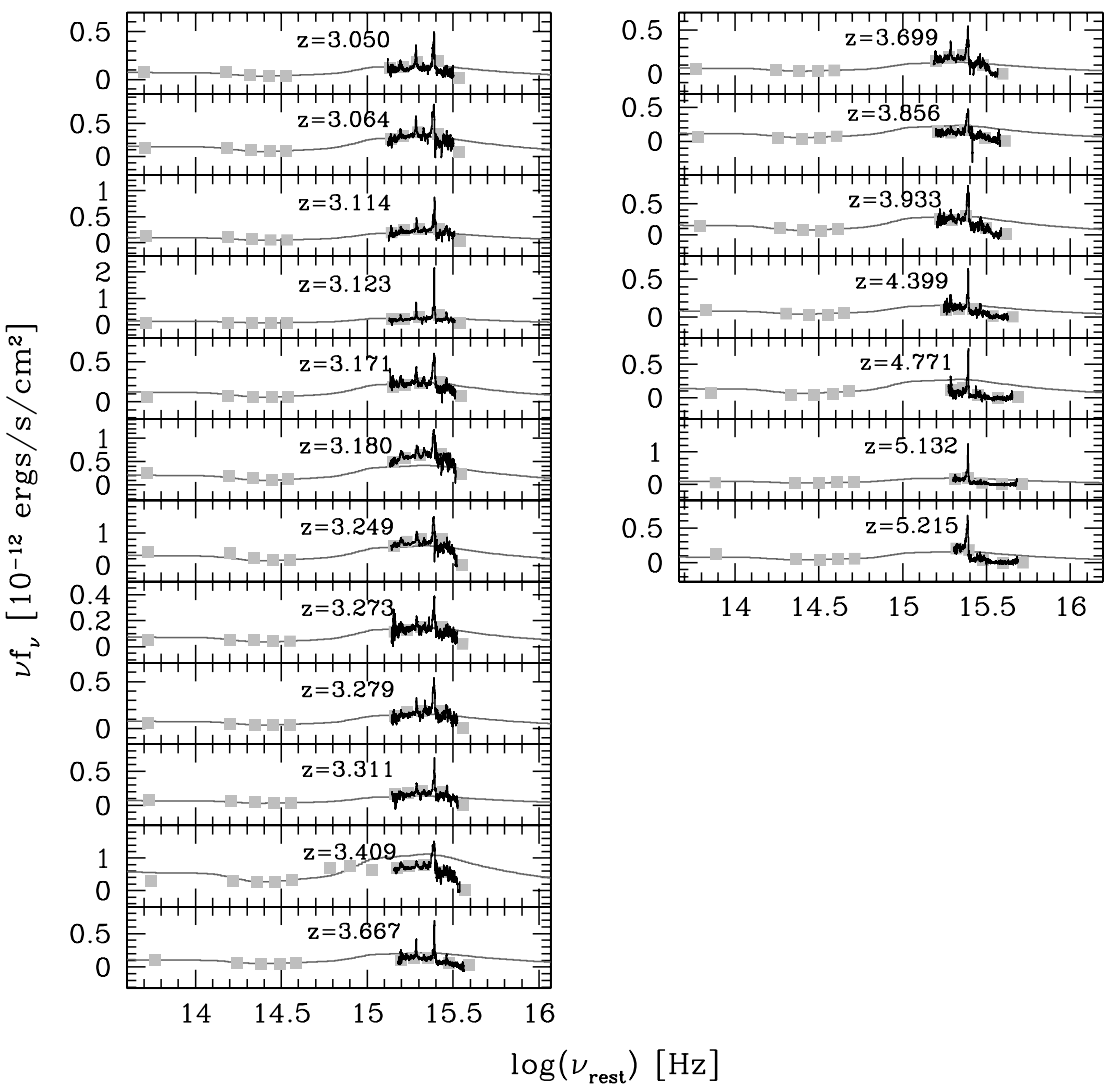

FIG. 14.—*Continued*

REFERENCES

Adelman-McCarthy, J. K., et al. 2006, ApJS, 162, 38
Antonucci, R. 1993, ARA&A, 31, 473
Avni, Y., & Tananbaum, H. 1986, ApJ, 305, 83
Becker, R. H., White, R. L., & Helfand, D. J. 1995, ApJ, 450, 559
Bianchi, L., et al. 2005, ApJ, 619, L27
Ciliegi, P., Zamorani, G., Hasinger, G., Lehmann, I., Szokoly, G., & Wilson, G. 2003, A&A, 398, 901
Ciliegi, P., et al. 1999, MNRAS, 302, 222
Condon, J. J., Cotton, W. D., Yin, Q. F., Shupe, D. L., Storrie-Lombardi, L. J., Helou, G., Soifer, B. T., & Werner, M. W. 2003, AJ, 125, 2411
Dullemond, C. P., & van Bemmel, I. M. 2005, A&A, 436, 47
Dunlop, J. S., McLure, R. J., Kukula, M. J., Baum, S. A., O'Dea, C. P., & Hughes, D. H. 2003, MNRAS, 340, 1095
Eisenhardt, P. R., et al. 2004, ApJS, 154, 48
Elitzur, M., Nenkova, M., & Ivesic, Z. 2003, preprint (astro-ph/0309040)
Elvis, M., et al. 1994, ApJS, 95, 1
Fabricant, D., et al. 2005, PASP, 117, 1411
Fadda, D., et al. 2006, AJ, AJ, 131, 2859
Fazio, G. G., et al. 2004, ApJS, 154, 10
Ferrarese, L. 2002, ApJ, 578, 90
Fioc, M., & Rocca-Volmerange, B. 1997, A&A, 326, 950
Frayer, D. T., et al. 2006, AJ, 131, 250
Fritz, J., Franceschini, A., & Hatziminaoglou, E. 2006, MNRAS, 366, 767
Fukugita, M., Ichikawa, T., Gunn, J. E., Doi, M., Shimasaku, K., & Schneider, D. P. 1996, AJ, 111, 1748
George, I. M., Turner, T. J., Yaqoob, T., Netzer, H., Laor, A., Mushotzky, R. F., Nandra, K., & Takahashi, T. 2000, ApJ, 531, 52
Glikman, E., Gregg, M. D., Lacy, M., Helfand, D. J., Becker, R. H., & White, R. L. 2004, ApJ, 607, 60
Glikman, E., Helfand, D. J., & White, R. L. 2006, ApJ, 640, 579
Gregg, M. D., Lacy, M., White, R. L., Glikman, E., Helfand, D., Becker, R. H., & Brotherton, M. S. 2002, ApJ, 564, 133
Hall, P. B., Green, R. F., & Cohen, M. 1998, ApJS, 119, 1
Hao, L., et al. 2005, AJ, 129, 1795
Hatziminaoglou, E., et al. 2005, AJ, 129, 1198
Jannuzi, B. T., & Dey, A. 1999, in ASP Conf. Ser. 191, Photometric Redshifts and the Detection of High Redshift Galaxies, ed. R. Weymann, L. Storrie-Lombardi, M. Sawicki, & R. Brunner (San Francisco: ASP), 111
Jester, S., et al. 2005, AJ, 130, 873
Kaspi, S., Maoz, D., Netzer, H., Peterson, B. M., Vestergaard, M., & Jannuzi, B. T. 2005, ApJ, 629, 61
Kaspi, S., Smith, P. S., Netzer, H., Maoz, D., Jannuzi, B. T., & Giveon, U. 2000, ApJ, 533, 631
Kuraszkiewicz, J. K., et al. 2003, ApJ, 590, 128
Lacy, M., et al. 2004, ApJS, 154, 166
———. 2005a, MmSAI, 76, 154
———. 2005b, ApJS, 161, 41
Lonsdale, C. J., et al. 2003, PASP, 115, 897
Martin, D. C., et al. 2005, ApJ, 619, L1
Martínez-Sansigre, A., Rawlings, S., Lacy, M., Fadda, D., Marleau, F. R., Simpson, C., Willott, C. J., & Jarvis, M. J. 2005, Nature, 436, 666
Nenkova, M., Ivezić, Ž., & Elitzur, M. 2002, ApJ, 570, L9
Papovich, C., et al. 2005, AJ, 132, 231
Peterson, B. M. 1997, An Introduction to Active Galactic Nuclei (Cambridge: Cambridge Univ. Press)
Polletta, M., Courvoisier, T. J.-L., Hooper, E. J., & Wilkes, B. J. 2000, A&A, 362, 75
Reeves, J. N., & Turner, M. J. L. 2000, MNRAS, 316, 234
Richards, G. T., et al. 2005, MNRAS, 360, 839
———. 2001, AJ, 122, 1151
———. 2002, AJ, 123, 2945
———. 2003, AJ, 126, 1131
———. 2004, ApJS, 155, 257
Rieke, G. H., et al. 2004, ApJS, 154, 25
Risaliti, G., & Elvis, M. 2004, in ASSL Vol. 308, Supermassive Black Holes in the Distant Universe, ed. A. J. Barger (Dordrecht: Kluwer), 187
Rowan-Robinson, M., et al. 2004, MNRAS, 351, 1290
Schlegel, D. J., Finkbeiner, D. P., & Davis, M. 1998, ApJ, 500, 525
Schneider, D. P., et al. 2005, AJ, 130, 367
Seibert, M., et al. 2005, ApJ, 619, L23
Skrutskie, M. F., et al. 1997, in The Impact of Large Scale Near-IR Sky Surveys, ed. F. Garzon et al. (Dordrecht: Kluwer), 25
Spergel, D. N., et al. 2003, ApJS, 148, 175
———. 2006, ApJ, submitted (astro-ph/0603449)
Steffen, A. T., et al. 2006, AJ, 131, 2826
Stern, D., et al. 2005, ApJ, 631, 163
Strateva, I. V., Brandt, W. N., Schneider, D. P., Vanden Berk, D. G., & Vignali, C. 2005, AJ, 130, 387
Surace, J., et al. 2005, http://swire.ipac.caltech.edu/swire/astronomers/publications/SWIRE2_doc_083105.pdf
Trammell, G. B., et al. 2005, BAAS, 207, 1812
Treister, E., et al. 2004, ApJ, 616, 123
———. 2006, ApJ, 640, 603
Tremaine, S., et al. 2002, ApJ, 574, 740
Ueda, Y., Akiyama, M., Ohta, K., & Miyaji, T. 2003, ApJ, 598, 886
van Bemmel, I. M., & Dullemond, C. P. 2003, A&A, 404, 1
Vanden Berk, D. E., et al. 2006, AJ, 131, 84
Voges, W., et al. 2000, IAU Circ., 7432, 3
Wandel, A., Peterson, B. M., & Malkan, M. A. 1999, ApJ, 526, 579
Weinstein, M. A., et al. 2004, ApJS, 155, 243
Werner, M. W., et al. 2004, ApJS, 154, 1
Wolf, C., Wisotzki, L., Borch, A., Dye, S., Kleinheinrich, M., & Meisenheimer, K. 2003, A&A, 408, 499
Wyder, T. K., et al. 2005, ApJ, 619, L15
York, D. G., et al. 2000, AJ, 120, 1579